Taylor & Francis
Taylor & Francis Group

ORIGINAL ARTICLE

Coupled field modelling of thermomechanical response in materials using peridynamic heat transport model and non-ordinary state-based peridynamics

Yakubu Kasimu Galadima[a,b], Selda Oterkus[a], and Erkan Oterkus[a]

[a]PeriDynamics Research Centre, Department of Naval Architecture, Ocean and Marine Engineering, University of Strathclyde, Glasgow, UK; [b]Department of Civil Engineering, Ahmadu Bello University, Zaria, Nigeria

ABSTRACT

Predicting the mechanical response of materials subjected to transient heat processes is crucial in various engineering applications. This paper introduces a novel peridynamic (PD) coupled field model formulated within the framework of Non-Ordinary State-Based Peridynamics (NOSBPD). This model offers the capability to simulate the coupled thermo-mechanical behavior of materials by incorporating both thermal transport and mechanical deformation analyses. To verify the model's accuracy, a benchmark problem involving a steel plate undergoing transient thermal expansion is investigated. This model presents a valuable tool for various engineering applications involving coupled thermo-mechanical processes.

1. Introduction

1.1. Motivation for the study

The coupling of thermal and mechanical fields is crucial in understanding the behavior of materials under various operational conditions, especially those involving extreme temperatures and mechanical loads. Thermomechanical coupling is particularly significant in applications such as aerospace, nuclear reactors, and electronic devices, where materials are subjected to high thermal gradients and mechanical stresses. Traditional continuum mechanics approaches often face limitations in accurately predicting fracture and damage in these scenarios due to their inability to naturally handle discontinuities and evolving cracks. Peridynamic (PD) theory, with its nonlocal formulation, offers a robust alternative by using integro-differential equations to model the behavior of materials, making it particularly successful at handling discontinuities.

In this study, we focus on advancing the state-of-the-art in coupled field modeling by developing a thermomechanical correspondence model within the framework of non-ordinary state-based peridynamics (NOSB-PD) and coupling it with an existing peridynamic thermal model. This work aims to address critical gaps in the current literature by formulating a framework that allows the integration of constitutive models from classical continuum mechanics (CCM) into the PD framework. This integration aims to accurately model thermal and mechanical responses, including the complex interaction effects between these fields.

The industrial applications of this study are vast and significant. In the aerospace industry, materials are often exposed to extreme temperatures and mechanical loads, leading to thermomechanical deformation and the potential for crack initiation and propagation. Accurately predicting these behaviors is crucial for the safety and reliability of aerospace components. In nuclear reactors, materials are subjected to high thermal gradients and radiation, which can cause thermal stresses and lead to crack formation. Understanding these processes is essential for maintaining the structural integrity of reactor components. Similarly, in the electronics industry, devices experience high thermal loads during operation, which can cause thermomechanical stresses and result in the formation of cracks in solder joints and other critical components. By applying our advanced thermomechanical correspondence model within the NOSB-PD framework, we can provide more accurate predictions of these behaviors, thereby improving the design and durability of industrial components subjected to harsh operating conditions.

1.2. Review of literature

A critical review of existing studies reveals several significant contributions in the field of thermomechanical modeling using PD. A coupled thermo-mechanical BBPD model was proposed in [1] to simulate thermal cracking in rocks. This framework integrates both heat conduction and mechanical deformation, providing a comprehensive approach to understanding how thermal stresses can lead to crack initiation and propagation in geological materials. The formulation

considers the thermal expansion effects and the transfer of heat within the rock, allowing for the accurate prediction of crack paths influenced by temperature gradients.

In [2], a NOSBPD formulation for thermoplastic fracture was developed, utilizing the Johnson-Cook constitutive model. This approach is particularly effective for simulating the behavior of materials under high strain rates and elevated temperatures. The Johnson-Cook model captures the effects of strain hardening, strain rate sensitivity, and thermal softening, making it suitable for materials experiencing dynamic loading conditions. An adaptive thermo-mechanical PD model for fracture analysis in ceramics was introduced in [3]. This OSBPD model employs adaptive grid refinement to enhance the resolution in critical areas where crack initiation and propagation are expected. The adaptive refinement technique improves computational efficiency by focusing computational resources on regions with high stress concentrations, thereby increasing the accuracy of the fracture predictions without significantly increasing the overall computational cost.

An axisymmetric OSBPD model for thermal cracking of linear elastic solids was presented in [4]. This model incorporates the effects of thermal expansion and bond failure criteria for analyzing thermal cracking in materials with rotational symmetry. The axisymmetric formulation simplifies the computational model while still capturing the essential physics of thermal cracking. This approach is beneficial for studying materials such as cylindrical rods or spherical shells, where the symmetry can be exploited to reduce computational effort while maintaining accuracy in the prediction of thermal stress induced.

A fully coupled PD thermomechanics model was derived in [5] to address transient scenarios involving complex thermal and mechanical interactions within the BBPD framework. In [6], a coupled thermo-mechanical BBPD framework was proposed to simulate thermomechanical fracture in inhomogeneous ice. This model considers the temperature sensitivity and the microstructural inhomogeneities of the ice, which are critical factors in accurately predicting fracture behavior. The study in [7] investigated the fracture mechanical behavior of granite containing a single fissure after thermal cycling treatment using a fully coupled OSBPD method. This approach integrates both thermal and mechanical fields to simulate the stress–strain response and crack evolution in granite subjected to repeated thermal loading. The OSBPD framework effectively captures the interaction between thermal cycling and mechanical fracture, providing insights into the durability and failure mechanisms of granite under such conditions.

Thermally induced fracture analysis of polycrystalline materials was explored in [8], focusing on the effects of grain size, grain boundary strength, and material composition. This study employed BBPD to investigate how thermal stresses lead to crack initiation and propagation within polycrystalline structures. By considering different grain sizes and boundary strengths, the model provides insights into how microstructural features influence the fracture behavior of polycrystalline materials under thermal loading. In [9], a

thermomechanical PD model for ductile fracture at high temperatures was proposed, incorporating a plastic bond constitutive model. This model addresses the behavior of ductile materials, which undergo significant plastic deformation before fracture, by integrating thermal effects with plasticity. The BBPD framework is used to simulate the high-temperature conditions that lead to ductile fracture, providing valuable insights into material performance and failure under extreme conditions.

The phase change the peridynamic model for welding analysis presented in [10] developed a non-linear transient PD model that incorporates phase transformation and various heat source models. This BBPD approach is designed to simulate the complex thermal processes involved in welding, including the melting and solidification of materials. By modeling the heat input from different sources and the resulting phase changes, the model accurately predicts the temperature distribution and mechanical responses during welding. Thermomechanics of damage in brittle solids was addressed in [11], presenting a fully coupled thermomechanical PD model that integrates thermal and mechanical fields. This NOSBPD model captures the damage evolution in brittle materials subjected to thermal and mechanical loads.

An OSBPD model for fully coupled thermoelastic problems was developed in [12], incorporating thermal expansion and bond failure criteria. The objective to simulate the coupled thermal and elastic responses of materials, providing a detailed analysis of how thermal loads induce elastic deformation and potentially lead to failure. In [13], a bond-based fully coupled thermomechanical PD framework was used to analyze fracture toughening mechanisms of stop holes in brittle materials. This study focuses on the role of stop holes in enhancing the fracture toughness of brittle materials under thermomechanical loads. The BBPD model captures the stress distribution around stop holes and predicts how they influence crack initiation and propagation, providing insights into the design of more resilient materials. PD was extended in [14] to predict damage initiation and propagation in electronic packages. This BBPD model integrates thermal and mechanical fields to simulate the complex loading conditions experienced by electronic components.

1.3. Contribution of the present study

Despite these advancements, significant gaps in the literature remain unaddressed. Many existing studies have predominantly focused on bond-based formulations, which, while useful, are limited in their ability to capture complex material behaviors when compared to state-based models. Specifically, the integration of constitutive models from CCM into the PD framework remains underexplored, particularly concerning thermomechanical response. This gap is evident in the literature survey, which highlights the need for a more robust approach.

This study aims to fill these gaps by proposing a novel thermomechanical correspondence framework within the

NOSBPD theory and coupling it with a PD thermal model [15]. The proposed framework takes a novel path by utilizing the generalized Hooke's law for linear thermoelectricity as the constitutive model, marking a departure from the thermoplasticity model employed in [2] and the specific constitutive model used in [11]. By leveraging a well-established constitutive model such as linear thermoelasticity, the framework benefits from the extensive validation and reliability that Hooke's law offers.

Furthermore, this study introduces the implicit formulation of the NOSBPD thermomechanical model for the first time. This implicit formulation is derived and implemented to simulate the thermoelastic response of materials, offering a computationally efficient framework. By addressing these gaps, the proposed framework aims to enhance the predictive capabilities of PD models in capturing the complex interactions between thermal and mechanical fields, thereby providing a more comprehensive tool for analyzing the thermomechanical behavior of materials.

2. Peridynamic mechanical model

PD [16] distinguishes itself from classical continuum mechanics through its departure from the traditional utilization of differential operators in the governing equations of motion. Instead, PD introduces integral operators, signifying a paradigmatic departure in the methodology of material modeling. This distinctive characteristic has profound implications, granting PD with several key advantages that enables it to transcend the constraints inherent in differential operators and classical continuum theories.

Firstly, the nonlocal nature inherent to the integral formulation renders PD intrinsically crack-compatible. Discontinuities no longer pose a challenge but are instead treated as the natural outcomes of the interactions between material points across crack surfaces. This crack-tolerance allows PD to seamlessly model fracture initiation and propagation [17–19] without resorting to ad-hoc crack growth algorithms, which is a stark contrast to classical methods.

The second key advantage that PD offers lies in its nonlocal formalism which is introduced through the concept of a horizon. This horizon defines the spatial extent over which interactions between material points occur. Unlike classical models, where interactions are confined to neighboring points, PD allows interactions to extend beyond localized regions.

However, it is important to note that the nonlocal nature of PD introduces a computational cost that is generally higher compared to frameworks based on local theories, such as the finite element method (FEM). This increased computational demand is due to the need to consider interactions over a broader spatial domain. Despite this setback, the advantages offered by PD, particularly its natural handling of discontinuities and robust fracture modeling capabilities, often compensate for the higher computational expense. Thus, PD represents a powerful tool in the field of material modeling, providing unique solutions to problems that are challenging for classical methods.

The horizon plays a pivotal role in capturing displacement localization [20], wherein materials exhibit concentrated deformation or strain softening behavior as deformation increases. This behavior is inherently difficult to model accurately using classical continuum mechanics without resorting to ad hoc regularization techniques [21].

The peridynamic equation of motion for a point $\mathbf{x}$ within a body $\boldsymbol{B}$, interacting with other points $\mathbf{x}'$ within $\boldsymbol{B}$, is formulated through the following balance of linear momentum expression:

$$\rho(\boldsymbol{x})\ddot{\boldsymbol{u}}(\mathbf{x}, t) = \int_{\mathcal{H}_\mathbf{x}} \mathbf{f}_m(\mathbf{x}, \mathbf{x}', t)dV_{\mathbf{x}'} + \mathbf{b}(\mathbf{x}, t) \qquad (1)$$

Equation (1) captures the governing dynamics of the system, incorporating familiar components like material density ρ and acceleration represented by the second-order displacement derivative $\ddot{\boldsymbol{u}}$. The nonlocal influence is introduced through the response function $\mathbf{f}_m(\mathbf{x}, \mathbf{x}', t)$, which is a pairwise force density function that is transmitted through the notion of a *bond*. This bond represents the interaction between two material points $\mathbf{x}$ and $\mathbf{x}'$, separated by a finite distance $\mathbf{x}' - \mathbf{x} = \xi$, termed the *bond length* in the undeformed configuration. The subscript m on the response function indicate that it pertains to mechanical model. The interaction region for each point $\mathbf{x}$ is defined by the region laying within limiting distance δ, often called the horizon of $\mathbf{x}$. The interaction region is typically taken to a be a sphere of radius δ. The set, $\mathcal{H}_\mathbf{x}$ of points located within the domain of interaction of $\mathbf{x}$ is called the family of $\mathbf{x}$.

As $\boldsymbol{B}$ deforms such that points $\mathbf{x}$ and $\mathbf{x}'$ occupy new positions $\mathbf{y}$ and $\mathbf{y}'$ in the deformed configuration as shown in Figure 1, the relative displacement and relative position vector of $\mathbf{x}$ and $\mathbf{x}'$ are respectively given as:
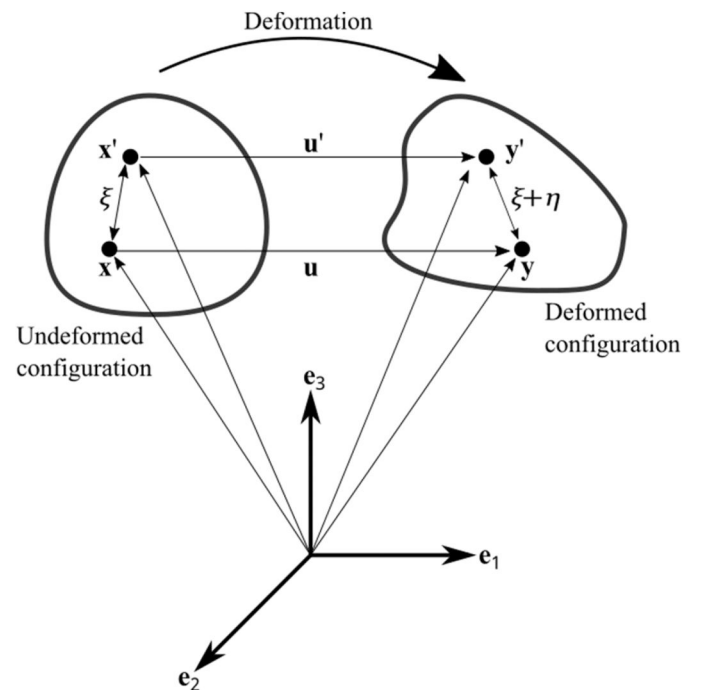

Figure 1. Deformation of material point.

$$\boldsymbol{\eta} = \boldsymbol{u}' - \boldsymbol{u}, \quad \boldsymbol{y}' - \boldsymbol{y} = \boldsymbol{\xi} + \boldsymbol{\eta} \tag{2}$$

Two broad class of PD models emerge from the definition of the force density function $\mathbf{f}(\boldsymbol{x}, \boldsymbol{x}', t)$ in (1). The first peridynamic model, known as the bond-based model [16], characterizes $\mathbf{f}(\boldsymbol{x}, \boldsymbol{x}', t)$ as only dependent on the bond $\mathbf{x}' - \mathbf{x}$, independent of the deformation of any other bond within the family of the primary point $\mathbf{x}$. This definition simplifies the peridynamic model, making it computationally efficient. However, it imposes constraints on the types of materials that can be modeled, limiting them to those with Poisson's ratio of 1/3 and 1/4 for problems in the 2- and 3-dimensions, respectively.

To overcome these limitations, a state-based peridynamic framework was introduced [22], offering more generalized capabilities for material modeling. In the state-based framework, the force density $\mathbf{f}(\boldsymbol{x}, \boldsymbol{x}', t)$ is not solely a function of the bond $\boldsymbol{x}' - \boldsymbol{x}$ but encompasses all bonds within $\mathcal{H}_x$. This enhanced capability arises from the introduction of mathematical objects called states, enabling the reformulation of the peridynamic equation of motion (1) as follows:

$$\rho(\mathbf{x})\ddot{\boldsymbol{u}}(\mathbf{x}, t) = \int_{\mathcal{H}_x} \left(\underline{\mathbf{T}}\,[\mathbf{x}, t]\langle\mathbf{x}' - \mathbf{x}\rangle - \underline{\mathbf{T}}\,[\mathbf{x}', t]\langle\mathbf{x} - \mathbf{x}'\rangle \right) dV_{\mathbf{x}'} + \mathbf{b}(\mathbf{x}, t) \tag{3}$$

In (3), $\underline{\mathbf{T}}\,[\mathbf{x}, t]$ and $\underline{\mathbf{T}}\,[\mathbf{x}', t]$ represent the vector force states acting at points $\mathbf{x}$ and $\mathbf{x}'$, respectively, at time t. The action of $\underline{\mathbf{T}}$ on the bonds $\mathbf{x}' - \mathbf{x}$ and $\mathbf{x} - \mathbf{x}'$ results in the generation of the vector-valued force density functions $\mathbf{t}(\mathbf{x}, \mathbf{x}', t)$ and $\mathbf{t}(\mathbf{x}', \mathbf{x}, t)$ acting on $\mathbf{x}$ and $\mathbf{x}'$, respectively. The bond which is acted upon a state is placed in an angle bracket.

Within the state-based framework (Eq. 3), two distinct material models emerge based on the definition of the force state $\underline{\mathbf{T}}$. If $\underline{\mathbf{T}}$ is defined such that the force density vector $\mathbf{t}$ aligns with the bond $\boldsymbol{\xi}$, $\underline{\mathbf{T}}$ is categorized as an ordinary state, leading to the formation of the ordinary state-based peridynamic (OSBPD) model. Alternatively, if $\underline{\mathbf{T}}$ does not align with the bond, it is deemed a non-ordinary state, giving rise to the Non-Ordinary State-Based Peridynamic (NOSBPD) model.

Within the NOSBPD framework, a crucial subclass known as the peridynamic correspondence model takes a fundamental role in significantly expanding the applicability of peridynamic theory. The correspondence model within the NOSBPD not only broadens the scope of modeling capabilities, inherent in the NOSBPD, but also introduces an essential feature – the integration of constitutive models from CCM framework into the peridynamic framework.

This key feature enables the correspondence model to leverage the rich legacy of CCM, with decades of research in calibration, verification and validation, and the advantages offered by peridynamics. The ability to incorporate well-established constitutive models from classical continuum mechanics into the peridynamic correspondence model enhances its versatility and reliability. By leveraging the state-of-the-art methodologies of CCM, the correspondence model benefits from a wealth of knowledge and testing that ensures robustness and accuracy in representing material. In the correspondence model, the net force state at a material point $\mathbf{x}$ is expressed as

$$\underline{\mathbf{T}}\,\langle\boldsymbol{\xi}\rangle = \omega\,(|\boldsymbol{\xi}|)\mathbf{P}\mathbf{B}\boldsymbol{\xi} \tag{4}$$

where ω is a scalar-valued weight function, $\mathbf{P} = \hat{\mathbf{P}}(\mathbf{F})$ represents the first Piola-Kirchhoff stress tensor, obtained through the material model $\hat{\mathbf{P}}$ derived from CCM, expressed as a function of the deformation gradient $\mathbf{F}$. The relationship between the First Piola-Kirchhoff stress $\mathbf{P}$ and the Cauchy stress tensor $\boldsymbol{\sigma}$ is established through the following expression:

$$\boldsymbol{P} = J\boldsymbol{\sigma}\mathbf{F}^{-T}, \quad J = det(\mathbf{F}) \tag{5}$$

Under small perturbation hypothesis, we have $\mathbf{F} \cong \mathbf{I}$, $J \cong 1$ and thus $\mathbf{P} = \boldsymbol{\sigma}$ in (5) and therefore (4) can be written as

$$\underline{\mathbf{T}}\,[\mathbf{x}, t]\langle\boldsymbol{\xi}\rangle = \omega(|\boldsymbol{\xi}|)\boldsymbol{\sigma}\mathbf{B}\boldsymbol{\xi} \tag{6}$$

where $\mathbf{B}$ in (4) and (6) is the inverse of a tensor-valued function called *shape tensor* $\mathbf{K}$ which is defined as.

$$\mathbf{K} = \int_{\mathcal{H}_x} \omega\,\langle\boldsymbol{\xi}\rangle\boldsymbol{\xi} \otimes \boldsymbol{\xi}\,dV_{\xi} \tag{7}$$

Instability in the displacement field often manifests in the correspondence model due to the inability of the nonlocal deformation gradient (7) to detect certain unphysical deformation modes. These unphysical deformation modes, also called zero-energy modes, need to be suppressed. Several techniques have been proposed to suppress the resultant instability. For reasons of ease of implementation, this study adopts the approach proposed in [23].

This method prevents zero-energy mode instability by adding an artificial force density vector $\underline{\mathbf{T}}^s[\mathbf{x}, t]\langle\mathbf{x}' - \mathbf{x}\rangle$ to the interaction between $\mathbf{x}$ and $\mathbf{x}'$ such that (6) becomes:

$$\underline{\mathbf{T}}\,[\mathbf{x}, t]\langle\boldsymbol{\xi}\rangle = \omega(|\boldsymbol{\xi}|)\boldsymbol{\sigma}\mathbf{B}\boldsymbol{\xi} + \underline{\mathbf{T}}^s[\boldsymbol{x}, t]\langle\mathbf{x}' - \mathbf{x}\rangle \tag{8}$$

where

$$\underline{\mathbf{T}}^s[\mathbf{x}, t]\langle\mathbf{x}' - \mathbf{x}\rangle = -\boldsymbol{\sigma}^s\mathbf{B}\boldsymbol{\xi} + \frac{1}{2}\omega\,\langle|\boldsymbol{\xi}|\rangle\mathbf{C}\,\underline{z}\,\langle\boldsymbol{\xi}\rangle \tag{9}$$

In (9), $\mathbf{C}(\boldsymbol{\xi}) = c(\boldsymbol{\xi} \otimes \boldsymbol{\xi})/|\boldsymbol{\xi}|^3$ is a tensor-valued symmetric micromodulus function where $c = 18k/\pi\delta^4$, and $\boldsymbol{\sigma}^s$

$$\boldsymbol{\sigma}^s = \frac{1}{2}\int_{\mathcal{H}_x} \omega\,\langle|\boldsymbol{\eta}|\rangle\mathbf{C}\langle\boldsymbol{\eta}\rangle\,\underline{z}\,\langle\boldsymbol{\eta}\rangle \otimes \boldsymbol{\eta}\,dV_{\boldsymbol{\eta}} \tag{10}$$

Under the assumption of a linear elastic material response within the correspondence model, we can employ the generalized Hooke's law as a constitutive model, establishing a relationship between the stress tensor in (6) and the strain tensor. The generalized Hooke's law, based on the small perturbation hypothesis, for the coupled thermoelastic problem is expressed as:

$$\begin{cases} \boldsymbol{\sigma}(\mathbf{x}, t) = \mathbb{C} \; : \; \boldsymbol{\varepsilon}(\mathbf{x}, t) - \boldsymbol{\beta}\Delta\Theta \\ \sigma_{ij} = \mathbb{C}_{ijkl}\varepsilon_{kl} - \beta_{ij}\Delta\Theta \qquad i, j, k, l \in \{1, 2, 3\} \end{cases} \tag{11}$$

where $\mathbb{C}$ is the fourth-order elastic constitutive tensor, $\boldsymbol{\beta}$ is a second-order constitutive thermal tensor and $\Delta\Theta = \Theta - \Theta_0$ is the change in temperature as represented by the difference between the absolute temperature θ at time t and the temperature at a reference state Θ_0. If the material is considered

isotropic, then $\mathbb{C}$ and $\boldsymbol{\beta}$ are isotropic fourth order and second order tensors which are respectively given as:

$$
\begin{cases}
\mathbb{C} = 3\kappa I_1 + 2\mu I_2 \text{ where } I_1 = \frac{1}{3}\delta_{ij}\delta_{kl}, \text{ and } I_2 = \frac{1}{2}\left(\delta_{ik}\delta_{jl} + \delta_{il}\delta_{jk} - \frac{2}{3}\delta_{ij}\delta_{kl}\right) \\
\quad \boldsymbol{\beta} = \beta \mathbf{1} \qquad\qquad\qquad\qquad \beta_{ij} = \beta\delta_{ij}
\end{cases}
$$

$$(12)$$

where κ and μ are the bulk and shear moduli, respectively, and β is a scalar thermal constant parameter that is given by

$$\beta_{ij} = \alpha_i \mathbb{C}_{ijkl}\delta_{ij} \tag{13}$$

where α_i is the thermal expansion coefficient in the i-th direction. The infinitesimal strain tensor $\boldsymbol{\varepsilon}$ in (11) is given by

$$\boldsymbol{\varepsilon}(\boldsymbol{x}) = \frac{1}{2}(\mathbf{F} + \mathbf{F}^T) - \mathbf{I} \tag{14}$$

and $\mathbf{F}$ is the nonlocal deformation gradient given by the approximate expression:

$$\mathbf{F}(\mathbf{x}) = \left[\int_{\mathcal{H}_{\mathbf{x}}} \underline{\omega}\langle\boldsymbol{\xi}\rangle \big(\mathbf{y}(\mathbf{x}',t) - \mathbf{y}(\mathbf{x},t)\big) \otimes \boldsymbol{\xi} d\mathbf{x}'\right]\mathbf{K}^{-1} \tag{15}$$

2.1. Numerical implementation of the correspondence model

To numerically solve the governing field equation (Eq. 3), the problem domain undergoes discretization into a set of nodes. Subsequently, frameworks such as the Finite Element Method (FEM) [24, 25], meshfree methods [26, 27], and collocation methods [28, 29], are employed to approximate the solution. In this contribution, the meshfree method [27] is adopted due to its straightforward implementation algorithm and relatively low computational cost. Employing this approximation method leads to the discrete form of (3), expressed as:

$$\rho_p \ddot{\mathbf{u}}_p = \sum_{q=1}^{N} \left[\underline{\mathbf{T}}\left[\mathbf{x}_p, t\right]\langle\mathbf{x}_q - \mathbf{x}_p\rangle - \underline{\mathbf{T}}\left[\mathbf{x}_q, t\right]\langle\mathbf{x}_p - \mathbf{x}_q\rangle\right]V_q + \mathbf{b}_p \tag{16}$$

where N denotes the number of nodes in the family of $\mathbf{x}_p$.

Two approaches exist to obtain the solution of the discretized PD equation of state (Eq. 16). The first is *via* an explicit time integration and the second is through implicit solution. The implicit solution strategy is utilized in this study. Different implicit strategies [30, 31] have been proposed for the solution of (16). We adopt the implicit strategy proposed in [31]. In this methodology, the discrete form of (8) is given by

$$
\begin{aligned}
\underline{\mathbf{T}}\left[\mathbf{x}_p, t\right]\langle\mathbf{x}_q - \mathbf{x}_p\rangle = {}& \underline{\omega}\langle\boldsymbol{\xi}_{pq}\rangle\boldsymbol{Q}_{pq}[\boldsymbol{C}\boldsymbol{B}_p\boldsymbol{N}_p\boldsymbol{U}_p] \\
& - \underline{\omega}\langle\boldsymbol{\xi}_{pq}\rangle\frac{c}{2}\boldsymbol{T}_{pq}\boldsymbol{R}_p\boldsymbol{P}_p\boldsymbol{U}_p \\
& + \underline{\omega}\langle\boldsymbol{\xi}\rangle\frac{c}{2}\big(\boldsymbol{B}_p\boldsymbol{\xi}_{pq}\big)_{d\times 2d}(\boldsymbol{V}_{pq}\boldsymbol{L}_p\boldsymbol{N}_p\boldsymbol{U}_p)_{2d\times 1} \\
& + \underline{\omega}\langle\boldsymbol{\xi}_{pq}\rangle\frac{c}{2}\frac{\boldsymbol{\xi}_{pq}\otimes\boldsymbol{\xi}_{pq}}{\left|\boldsymbol{\xi}_{pq}\right|^3}\left(\mathbf{u}_q - \mathbf{u}_p\right) \\
& - \frac{c}{2}\boldsymbol{M}_{pq}\boldsymbol{L}_p\boldsymbol{N}_p\boldsymbol{U}_p - \underline{\omega}\langle\boldsymbol{\xi}\rangle\boldsymbol{\beta}_p\boldsymbol{Q}_{pq}\epsilon
\end{aligned}
$$

$$(17)$$

so that the equilibrium equation of state (16) becomes

$$
\begin{aligned}
\rho_p \ddot{\mathbf{u}}_p = \sum_{j=1}^{n_i} \Big[& \underline{\omega}\langle\boldsymbol{\xi}_{pq}\rangle\boldsymbol{Q}_{pq}[\boldsymbol{C}\boldsymbol{B}_p\boldsymbol{N}_p\boldsymbol{U}_p] - \underline{\omega}\langle\boldsymbol{\xi}_{pq}\rangle\frac{c}{2}\boldsymbol{T}_{pq}\boldsymbol{R}_p\boldsymbol{P}_p\boldsymbol{U}_p \\
& + \underline{\omega}\langle\boldsymbol{\xi}\rangle\frac{c}{2}\big(\boldsymbol{B}_p\boldsymbol{\xi}_{pq}\big)_{d\times 2d}(\boldsymbol{V}_{pq}\boldsymbol{L}_p\boldsymbol{N}_p\boldsymbol{U}_p)_{2d\times 1} \\
& + \underline{\omega}\langle\boldsymbol{\xi}_{pq}\rangle\frac{c}{2}\frac{\boldsymbol{\xi}_{pq}\otimes\boldsymbol{\xi}_{pq}}{\left|\boldsymbol{\xi}_{pq}\right|^3}\left(\mathbf{u}_q - \mathbf{u}_p\right) - \frac{c}{2}\boldsymbol{M}_{pq}\boldsymbol{L}_p\boldsymbol{N}_p\boldsymbol{U}_p \\
& - \underline{\omega}\langle\boldsymbol{\xi}_{pq}\rangle\boldsymbol{\beta}_p\boldsymbol{Q}_{pq}\epsilon - \underline{\omega}\langle\boldsymbol{\xi}_{qp}\rangle\boldsymbol{Q}_{qp}[\boldsymbol{C}\boldsymbol{B}_q\boldsymbol{N}_q\boldsymbol{U}_q] \\
& + \underline{\omega}\langle\boldsymbol{\xi}_{qp}\rangle\frac{c}{2}\boldsymbol{T}_{pq}\boldsymbol{R}_q\boldsymbol{P}_q\boldsymbol{U}_q \\
& - \underline{\omega}\langle\boldsymbol{\xi}_{qp}\rangle\frac{c}{2}\big(\boldsymbol{B}_q\boldsymbol{\xi}_{qp}\big)_{d\times 2d}(\boldsymbol{V}_{qp}\boldsymbol{L}_q\boldsymbol{N}_q\boldsymbol{U}_q)_{2d\times 1} \\
& - \underline{\omega}\langle\boldsymbol{\xi}_{qp}\rangle\frac{c}{2}\frac{\boldsymbol{\xi}_{qp}\otimes\boldsymbol{\xi}_{qp}}{\left|\boldsymbol{\xi}_{qp}\right|^3}\left(\mathbf{u}_p - \mathbf{u}_q\right) + \frac{c}{2}\boldsymbol{M}_{qp}\boldsymbol{L}_q\boldsymbol{N}_q\boldsymbol{U}_q \\
& + \underline{\omega}\langle\boldsymbol{\xi}_{qp}\rangle\boldsymbol{\beta}_q\boldsymbol{Q}_{qp}\epsilon\Big] + \mathbf{b}(\boldsymbol{x}_p)
\end{aligned}
$$

$$(18)$$

In the case of quasi-static problem, (18) specializes to

$$
\begin{aligned}
\sum_{j=1}^{n_i} \Big[& \underline{\omega}\langle\boldsymbol{\xi}_{pq}\rangle\boldsymbol{Q}_{pq}[\boldsymbol{C}\boldsymbol{B}_p\boldsymbol{N}_p\boldsymbol{U}_p] - \underline{\omega}\langle\boldsymbol{\xi}_{pq}\rangle\frac{c}{2}\boldsymbol{T}_{pq}\boldsymbol{R}_p\boldsymbol{P}_p\boldsymbol{U}_p \\
& + \underline{\omega}\langle\boldsymbol{\xi}\rangle\frac{c}{2}\big(\boldsymbol{B}_p\boldsymbol{\xi}_{pq}\big)_{d\times 2d}(\boldsymbol{V}_{pq}\boldsymbol{L}_p\boldsymbol{N}_p\boldsymbol{U}_p)_{2d\times 1} \\
& + \underline{\omega}\langle\boldsymbol{\xi}_{pq}\rangle\frac{c}{2}\frac{\boldsymbol{\xi}_{pq}\otimes\boldsymbol{\xi}_{pq}}{\left|\boldsymbol{\xi}_{pq}\right|^3}\left(\mathbf{u}_q - \mathbf{u}_p\right) - \frac{c}{2}\boldsymbol{M}_{pq}\boldsymbol{L}_p\boldsymbol{N}_p\boldsymbol{U}_p \\
& - \underline{\omega}\langle\boldsymbol{\xi}_{pq}\rangle\beta_p\boldsymbol{Q}_{pq}\epsilon - \underline{\omega}\langle\boldsymbol{\xi}_{qp}\rangle\boldsymbol{Q}_{qp}[\boldsymbol{C}\boldsymbol{B}_q\boldsymbol{N}_q\boldsymbol{U}_q] \\
& + \underline{\omega}\langle\boldsymbol{\xi}_{qp}\rangle\frac{c}{2}\boldsymbol{T}_{pq}\boldsymbol{R}_q\boldsymbol{P}_q\boldsymbol{U}_q \\
& - \underline{\omega}\langle\boldsymbol{\xi}_{qp}\rangle\frac{c}{2}\big(\boldsymbol{B}_q\boldsymbol{\xi}_{qp}\big)_{d\times 2d}(\boldsymbol{V}_{qp}\boldsymbol{L}_q\boldsymbol{N}_q\boldsymbol{U}_q)_{2d\times 1} \\
& - \underline{\omega}\langle\boldsymbol{\xi}_{qp}\rangle\frac{c}{2}\frac{\boldsymbol{\xi}_{qp}\otimes\boldsymbol{\xi}_{qp}}{\left|\boldsymbol{\xi}_{qp}\right|^3}\left(\mathbf{u}_p - \mathbf{u}_q\right) + \frac{c}{2}\boldsymbol{M}_{qp}\boldsymbol{L}_q\boldsymbol{N}_q\boldsymbol{U}_q \\
& + \underline{\omega}\langle\boldsymbol{\xi}_{qp}\rangle\boldsymbol{\beta}_q\boldsymbol{Q}_{qp}\epsilon\Big] + \mathbf{b}(\boldsymbol{x}_p) = 0
\end{aligned}
$$

$$(19)$$

The terms in Eq. (17) for two dimensions are specified [32] as follows: $\mathbf{Q}$ is a 2×3 matrix that captures the $\mathbf{B}\xi$ in (6) and is given [31] as

$$\mathbf{Q} = \begin{bmatrix} Q_1 & 0 & Q_2 \\ 0 & Q_2 & Q_1 \end{bmatrix} \tag{20}$$

where $Q_1 = B_{11}\xi_1 + B_{12}\xi_2$, $Q_1 = B_{12}\xi_1 + B_{22}\xi_2$. $\mathbf{D}$ is a matrix representation of the elasticity tensor. $\overline{\mathbf{K}}$ is a 3×4 matrix that is composed of components of $\mathbf{B}$, and is given by:

$$\overline{\mathbf{K}} = \begin{bmatrix} B_{11} & 0 & B_{12} & 0 \\ 0 & B_{12} & 0 & B_{22} \\ B_{12} & B_{11} & B_{22} & B_{12} \end{bmatrix} \tag{21}$$

$\boldsymbol{N}$ is a $4 \times 2(n+1)$ matrix which is given as:

$$\boldsymbol{N} = \begin{bmatrix} N^{(1)} & 0 & \cdots & \omega\xi_1 V_q & 0 & \cdots \\ 0 & N^{(1)} & \cdots & 0 & \omega\xi_1 V_q & \cdots \\ N^{(2)} & 0 & \cdots & \omega\xi_2 V_q & 0 & \cdots \\ 0 & N^{(2)} & \cdots & 0 & \omega\xi_1 V_q & \cdots \end{bmatrix} \tag{22}$$

where $N^{(1)} = -\sum_{q=1}^{n} \omega\left(\left|\boldsymbol{\xi}_{pq}\right|\right) \xi_{pq_1} V_q$, $\quad N^{(2)} = -\sum_{q=1}^{n}$ $\omega\left(\left|\boldsymbol{\xi}_{pq}\right|\right) \xi_{pq_2} V_q$. $\mathbf{U}$ is a vector of components of nodal displacements of points belonging to the family of point $\mathbf{x}_p$. $\mathbf{T}$ is given by

$$T = \begin{bmatrix} \xi_1 & \xi_2 & B_{12} & 0 \\ 0 & 0 & \xi_1 & \xi_2 \end{bmatrix} \quad (23)$$

R is given by:

$$R = \begin{bmatrix} B_{11} & B_{12} & 0 \\ B_{12} & B_{22} & 0 \\ 0 & B_{11} & B_{12} \\ 0 & B_{12} & B_{22} \end{bmatrix} \quad (24)$$

P is given as:

$$P = \begin{bmatrix} P^{(1)} & P^{(2)} & \cdots & \omega\xi_1^3/|\xi|^3 V_q & \omega\xi_1^2\xi_2/|\xi|^3 V_q & \cdots \\ P^{(2)} & P^{(3)} & \cdots & \omega\xi_1^2\xi_2/|\xi|^3 V_q & \omega\xi_1\xi_2^2/|\xi|^3 V_q & \cdots \\ P^{(3)} & P^{(4)} & \cdots & \omega\xi_1\xi_2^2/|\xi|^3 V_q & \omega\xi_2^3/|\xi|^3 V_q & \cdots \end{bmatrix} \quad (25)$$

where

$$P^{(1)} = -\sum_{q=1}^{n} \frac{\omega\langle|\xi|\rangle\xi_1^3}{|\xi|^3} V_q, \quad P^{(2)} = -\sum_{q=1}^{n} \frac{\omega\langle|\xi|\rangle\xi_1^2\xi_2}{|\xi|^3} V_q,$$

$$P^{(3)} = -\sum_{q=1}^{n} \frac{\omega\langle|\xi|\rangle\xi_1\xi_2^2}{|\xi|^3} V_q, \quad P^{(4)} = -\sum_{q=1}^{n} \frac{\omega\langle|\xi|\rangle\xi_2^3}{|\xi|^3} V_q,$$

L, V, M are respectively given by:

$$L = \begin{bmatrix} B_{11} & 0 & B_{12} & 0 \\ 0 & B_{12} & 0 & B_{22} \\ B_{12} & 0 & B_{22} & 0 \\ 0 & B_{11} & 0 & B_{12} \end{bmatrix} \quad (26)$$

$$V = \begin{bmatrix} \sum_{q=1}^{n}\omega\langle|\xi|\rangle\xi_1^4/|\xi|^3 V_q & \sum_{q=1}^{n}\omega\langle|\xi|\rangle\xi_1^2\xi_2^2/|\xi|^3 V_q & \sum_{q=1}^{n}\omega\langle|\xi|\rangle\xi_1^3\xi_2/|\xi|^3 V_q & \sum_{q=1}^{n}\omega\langle|\xi|\rangle\xi_1^3\xi_2/|\xi|^3 V_q \\ \sum_{q=1}^{n}\omega\langle|\xi|\rangle\xi_1^3\xi_2/|\xi|^3 V_q & \sum_{q=1}^{n}\omega\langle|\xi|\rangle\xi_1\xi_2^3/|\xi|^3 V_q & \sum_{q=1}^{n}\omega\langle|\xi|\rangle\xi_1^2\xi_2^2/|\xi|^3 V_q & \sum_{q=1}^{n}\omega\langle|\xi|\rangle\xi_1^2\xi_2^2/|\xi|^3 V_q \\ \sum_{q=1}^{n}\omega\langle|\xi|\rangle\xi_1^3\xi_2/|\xi|^3 V_q & \sum_{q=1}^{n}\omega\langle|\xi|\rangle\xi_1\xi_2^3/|\xi|^3 V_q & \sum_{q=1}^{n}\omega\langle|\xi|\rangle\xi_1^2\xi_2^2/|\xi|^3 V_q & \sum_{q=1}^{n}\omega\langle|\xi|\rangle\xi_1^2\xi_2^2/|\xi|^3 V_q \\ \sum_{q=1}^{n}\omega\langle|\xi|\rangle\xi_1^2\xi_2^2/|\xi|^3 V_q & \sum_{q=1}^{n}\omega\langle|\xi|\rangle\xi_2^4/|\xi|^3 V_q & \sum_{q=1}^{n}\omega\langle|\xi|\rangle\xi_1\xi_2^3/|\xi|^3 V_q & \sum_{q=1}^{n}\omega\langle|\xi|\rangle\xi_1\xi_2^3/|\xi|^3 V_q \end{bmatrix} \quad (27)$$

$$M = \begin{bmatrix} \xi_1^3/|\xi|^3 & \xi_1\xi_2^2/|\xi|^3 & \xi_1^2\xi_2/|\xi|^3 & \xi_1^2\xi_2/|\xi|^3 \\ \xi_1^2\xi_2/|\xi|^3 & \xi_2^3/|\xi|^3 & \xi_1\xi_2^2/|\xi|^3 & \xi_1\xi_2^2/|\xi|^3 \end{bmatrix} \quad (28)$$

And the product $\mathbf{B}\boldsymbol{\xi}$ is given by:

$$\mathbf{B}\boldsymbol{\xi} = \begin{bmatrix} B_{11}\xi_1 + B_{12}\xi_2 & B_{21}\xi_1 + B_{22}\xi_2 & 0 & 0 \\ 0 & 0 & B_{11}\xi_1 + B_{12}\xi_2 & B_{21}\xi_1 + B_{22}\xi_2 \end{bmatrix} \quad (29)$$

The term $\omega\langle\xi\rangle\dfrac{c}{2}\dfrac{\boldsymbol{\xi}\otimes\boldsymbol{\xi}}{|\xi|^3}\ (\mathbf{u'} - \mathbf{u})$ for example is evaluated as:

$$\underline{\omega}\langle\xi\rangle\frac{c}{2}\frac{\boldsymbol{\xi}\otimes\boldsymbol{\xi}}{|\xi|^3}\ (\mathbf{u'} - \mathbf{u}) = \frac{c}{2}\begin{bmatrix} \dfrac{\xi_1^2}{|\xi|^3}(u'-u)_1 + \dfrac{\xi_1\xi_2}{|\xi|^3}(u'-u)_2 \\ \dfrac{\xi_1\xi_2}{|\xi|^3}(u'-u)_1 + \dfrac{\xi_1^2}{|\xi|^3}(u'-u)_2 \end{bmatrix} \quad (30)$$

And finally, the constitutive thermal tensor $\boldsymbol{\beta}$ at point p is given in (13).

3. Peridynamic heat transport model

Incorporating the thermal component into our coupled framework necessitates the integration of a peridynamic heat conduction formulation. Analogous to the mechanical model, heat transfer within this framework is facilitated through non-local interactions among material points, constrained within a specified heat diffusion horizon.

Extensive research endeavors have been dedicated to the development and application of the PD framework for modeling heat transport phenomena, as evidenced by numerous studies [15, 33–40]. In this study, we adopt the PD heat transport model presented in [15]. The governing field equation for heat conduction in this formulation is expressed as:

$$\rho C_v \dot{\Theta}(\mathbf{x}, t) = \int_{\mathcal{H}_\mathbf{x}} f_h(\mathbf{x}, \mathbf{x'}, \Theta, \Theta', t) dV_{\mathbf{x'}} + h_s(\mathbf{x}, t) \quad \forall \mathbf{x} \in \Omega \quad (31)$$

where $f_h(\mathbf{x}, \mathbf{x'}, \Theta, \Theta', t)$ is the thermal response function and represent a heat flow density, h_s is the heat source due to volumetric heat generation [15], and Θ is the temperature

at $\mathbf{x}$. The thermal response function can be written in terms of a PD micro-conductivity κ as:

$$f_h = \kappa \, \frac{\tau(\mathbf{x}, \mathbf{x}', t)}{|\xi|} \tag{32}$$

Depending on the dimension of the problem, the PD micro-conductivity κ is shown to be related to the thermal conductivity k of the material through the following relations:

$$\kappa = \frac{2k}{A\delta^2} \quad \text{One-dimension}$$

$$\kappa = \frac{6k}{\pi h \delta^3} \quad \text{Two-dimension} \tag{33}$$

$$\kappa = \frac{6k}{\pi \delta^4} \quad \text{Three-dimension}$$

4. Numerical results

In this section, two numerical experiments will be conducted to demonstrate the capabilities of the proposed NOSBPD thermomechanical framework to accurately predict the response of materials subjected to mechanical and thermal loads.

4.1. Plate subjected to temperature boundary condition

In this example, a benchmark problem involving a plate undergoing transient thermal process and subsequent thermal expansion is studied. The plate, with dimension $l = 1\ m$ and $w = 0.5m$ as shown in Figure 2, is subjected to the following thermal initial and boundary conditions:
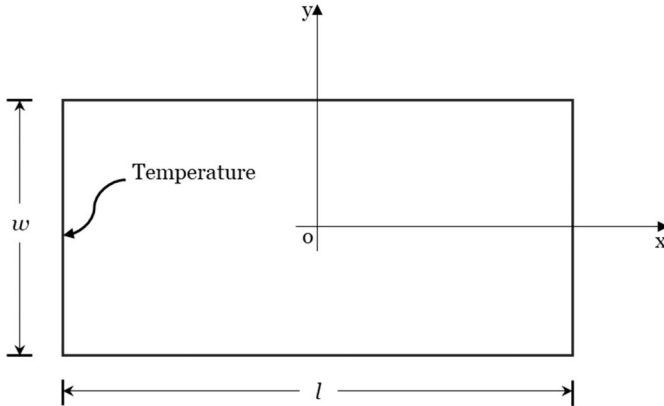
Figure 2. Problem setup for thermal conduction simulation.

$$T((\mathrm{x}, \mathrm{y}), 0) = 0°C \quad -l/2 \le \mathrm{x} \le l/2 \quad -w/2 \le \mathrm{y} \le w/2$$

$$T((x, y), t) = 900°C \quad \mathrm{x} = -l/2 \quad -w/2 \le \mathrm{y} \le w/2 \tag{34}$$

The properties of the plate material are as follows: elastic modulus of 200 GPa, Poisson's ratio of 1/3 and a coefficient of thermal expansion of 23×10^{-6}. The horizon of the material is taken as $3\Delta \mathrm{x}$, where $\Delta \mathrm{x} = \Delta \mathrm{y}$ is the space between material points in the discretized domain along its length and width. The plate is discretized into 201 material points along its length and 101 material points along its width.

First, a transient heat conduction analysis is performed using the peridynamic thermal conduction model over a simulation time of 3000s. This step determines the evolution of temperature distribution within the plate. Subsequently, this temperature distribution is used as input for a coupled thermomechanical simulation using Eq. (19). An additional prescribed homogeneous displacement boundary condition is applied at the right edge of the plate. The coupled PD thermomechanical model, incorporating both thermal and mechanical effects, then solves for the resulting displacements within the plate.

The evolution of the temperature distribution obtained from the simulation of the PD thermal transport model is depicted in Figures 3 and 4. Figure 3 illustrates the evolution of the temperature distribution over the entire plate at simulation times corresponding to 100 s, 1500 s, and 3000 s.

To compare the evolution of the temperature field obtained using the PD thermal transport model, the temperature along a grid located at $-\delta/10 \le \mathrm{y} \le \delta/10$ and $-l/2 \le \mathrm{x} \le l/2$ at time 100 s, 1500 s, and 3000 s are presented in Figure 4. This result is compared with result of simulation from ANSYS mechanical APDL, a commercial finite element software. From Figure 4, it is evident that the predictions from the PD transport model align well with those from ANSYS, indicating good agreement between the two.

The evolution of temperature gradient obtained from simulation of the PD thermal transport model serve as input for the subsequent simulation of the displacement field arising from thermal expansion. To this end, the capability of the proposed NOSBPD coupled field mode to account for thermo-mechanical interaction is leveraged. The evolution of the displacement field across the plate at simulation times of 100 s, 1500 s, and 3000 s is presented in Figures 5–7, respectively. These figures offer insights into the progressive deformation of the plate due to the transient thermal process.
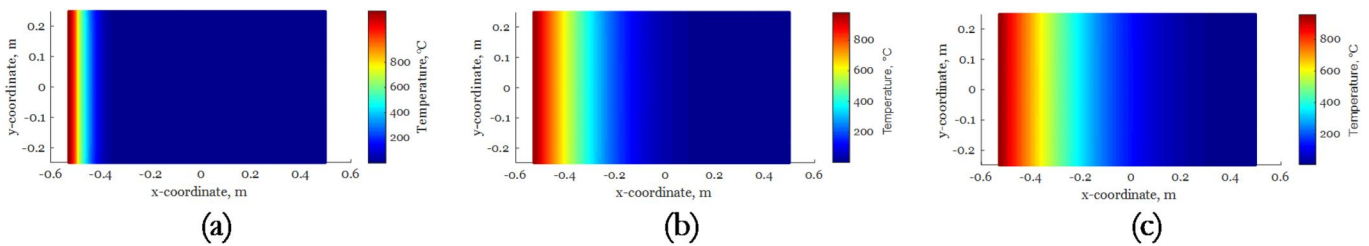

Figure 3. Evolution of temperature distribution at (a) t = 100 s, (b) t = 1500 s, and (c) t = 300 s.

To validate the accuracy of the PD coupled field model, a comparative analysis is conducted. The same problem is simulated using ANSYS. The resulting displacement field evolution for the plate at corresponding simulation times (100 s, 1500 s, and 3000 s) is presented alongside the PD model results in Figures 5–7. This allows for a direct visual comparison of the predicted deformations.
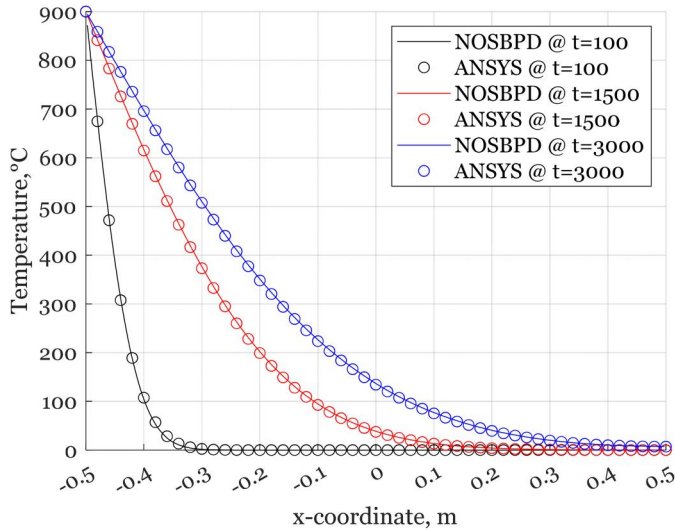

Figure 4. Temperature profile for material points located at $-\delta/10 \leq y \leq \delta/10$.

To facilitate a more precise comparison, the displacement profiles along grids parallel to the x and y axes, showing displacement components in the x and y directions obtained from simulations using the PD coupled field model and ANSYS, are presented in Figure 8.

The results obtained from simulating the proposed PD coupled field model show good agreement with the finite element simulation conducted using ANSYS, as presented in Figures 5–8. An examination of these results reveals a consistent trend in the evolution of the displacement field across both models. This agreement is observed at all three depicted simulation times of 100 s, 1500 s, and 3000 s, suggesting that the PD model effectively addresses the thermo-mechanical coupling within the material.

By demonstrating consistency with the results obtained from the established finite element simulations using ANSYS, our findings affirm the effectiveness of the proposed PD coupled field model in accurately representing the mechanical response of the system. This agreement between the simulated outcomes further validates the applicability of the PD coupled field model in engineering analyses involving thermomechanical processes.

4.2. Response of a plate with a slit subjected to elevated temperature

In this example, we simulate the response of a plate with a central slit, composed of a material with the following
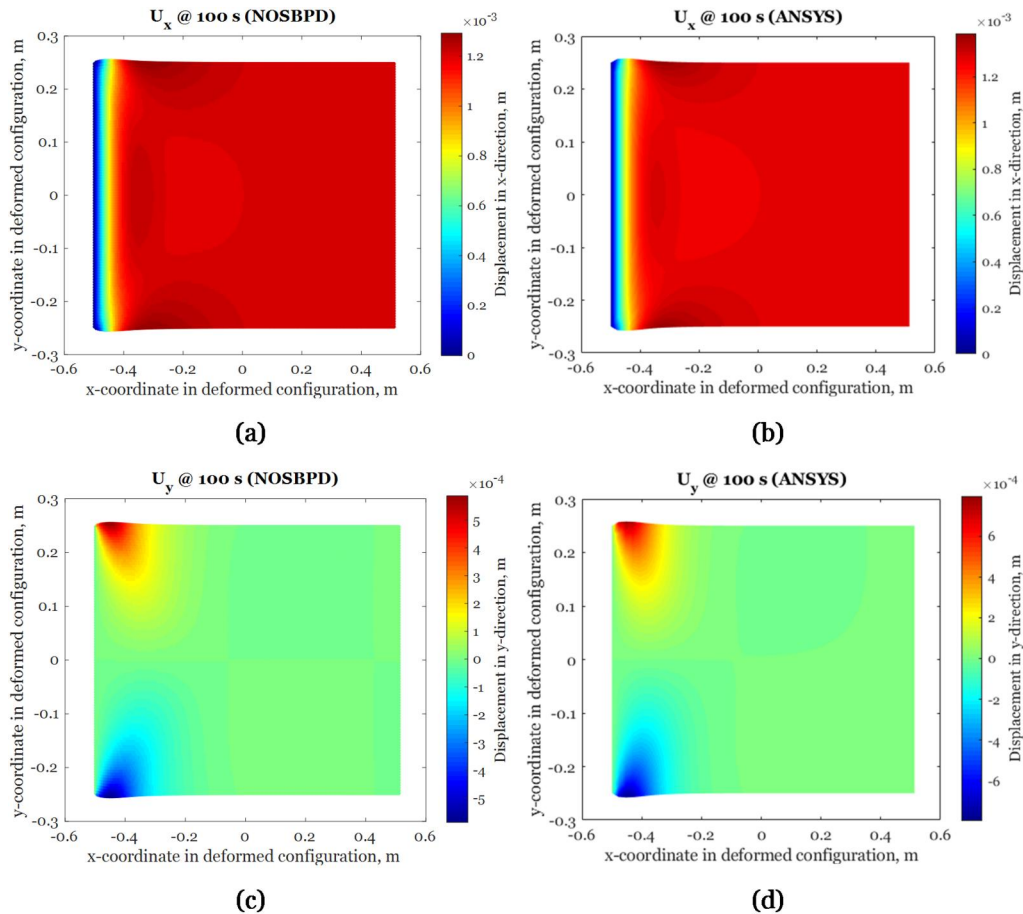
Figure 5. Components of displacement over the entire plate at 100 s (a) in x-direction obtained using NOSBPD, (b) in x-direction obtained using ANSYS, (c) in y-direction obtained using NOSBPD, and (d) in y-direction obtained using ANSYS.
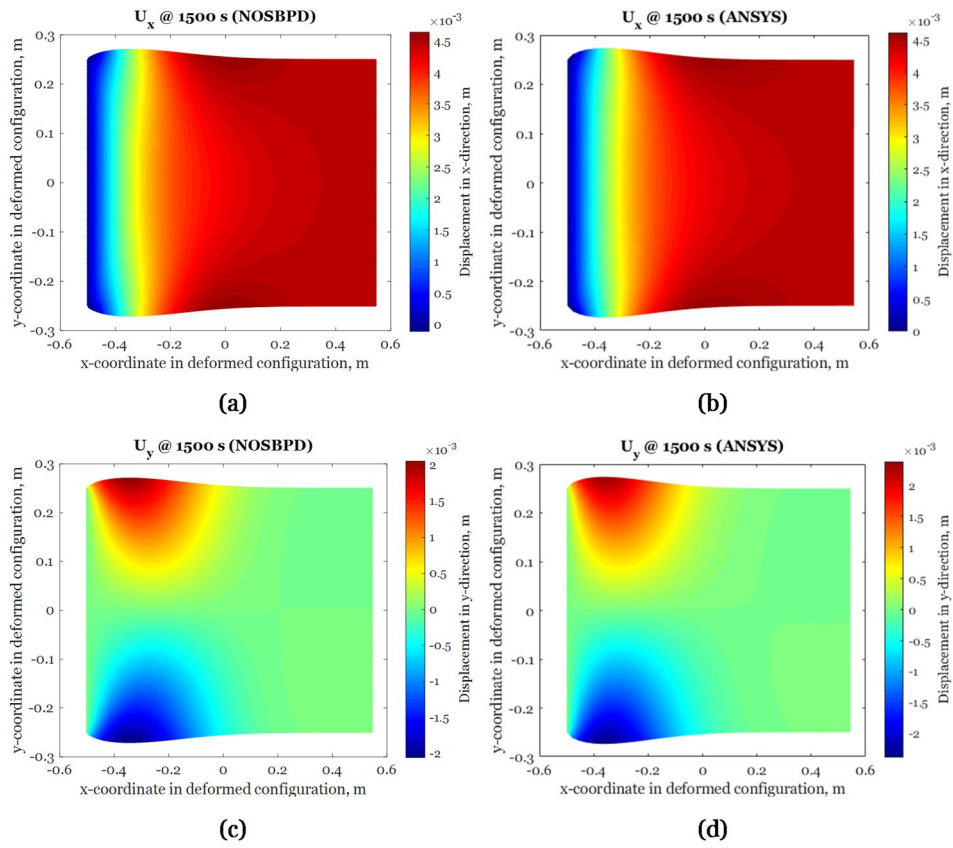
Figure 6. Components of displacement over the entire plate at 1500 s (a) in x-direction obtained using NOSBPD, (b) in x-direction obtained using ANSYS, (c) in y-direction obtained using NOSBPD, and (d) in y-direction obtained using ANSYS.
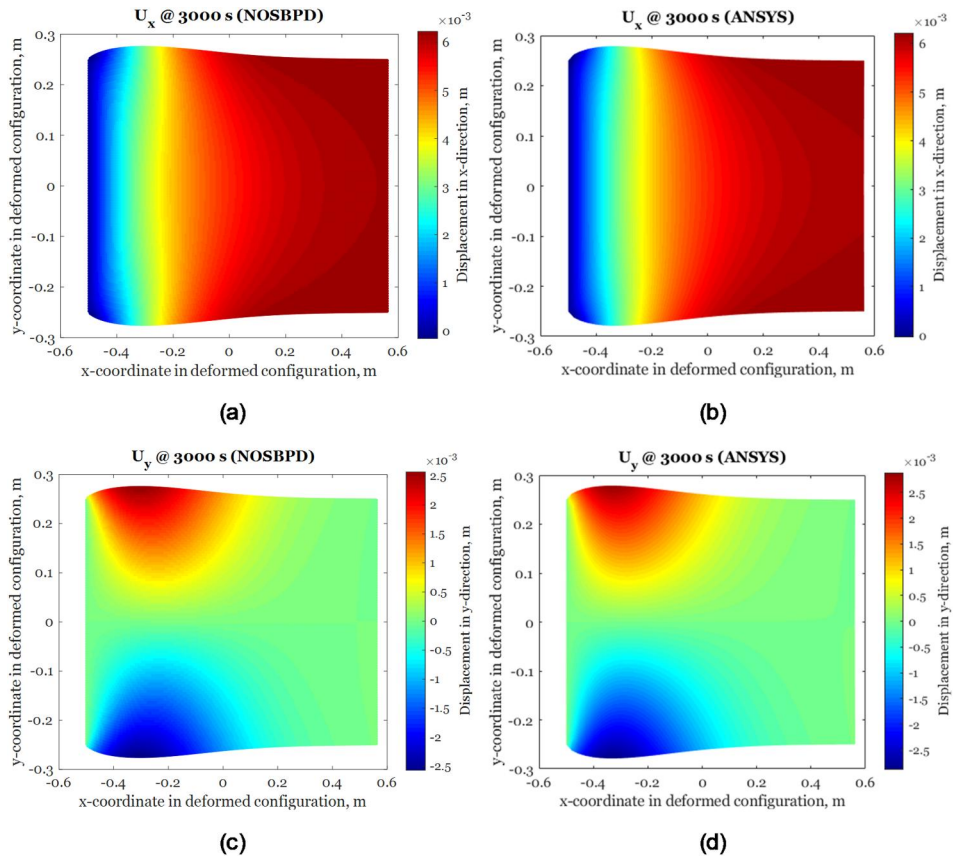
Figure 7. Components of displacement over the entire plate at 3000 s (a) in x-direction obtained using NOSBPD, (b) in x-direction obtained using ANSYS, (c) in y-direction obtained using NOSBPD, and (d) in y-direction obtained using ANSYS.
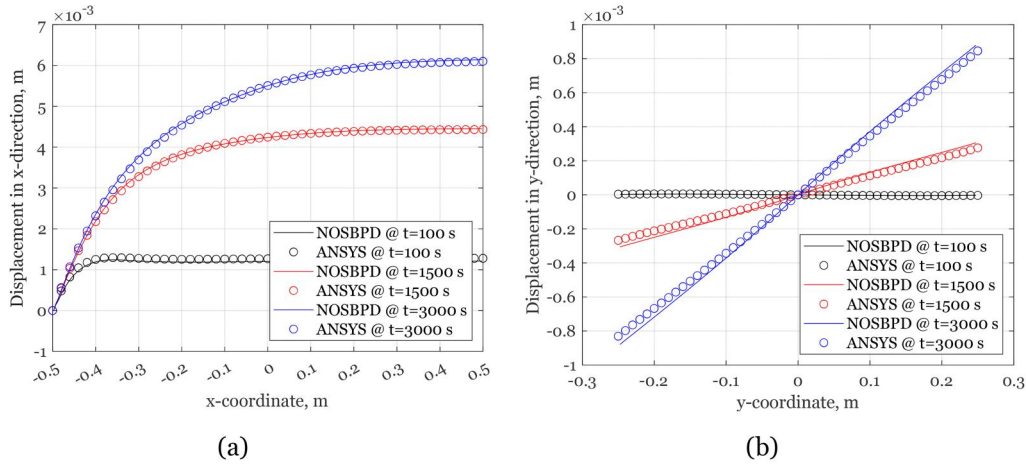
Figure 8. Displacement profile for material points located at $-\delta/10 \leq y \leq \delta/10$ and $-l/2 \leq x \leq l/2$.

mechanical properties: an elastic modulus of 35.8 GPa, a Poisson's ratio of 0.333, and a coefficient of thermal expansion of 23×10^{-6}. The primary objective of this numerical experiment is to demonstrate the capability of the proposed implicit thermomechanical framework in accurately modeling materials that feature discontinuities, such as cracks or slits, under thermal loading.

The plate is a rectangular slab with a length (L) and width (W) of 1 m. A central slit with dimensions of length (2a) of 0.4 m and height of 0.005 m is introduced to represent a discontinuity within the plate. To facilitate the numerical simulations, the plate is discretized into a grid of 301 material points along both its length and width, while a single layer of material points is used through its thickness, thus assuming a plane stress condition.

The bottom edge of the plate is fixed, restricting both horizontal and vertical displacements. A uniform displacement is prescribed along the top edge of the plate, with an applied displacement of 0.005 m. Additionally, the plate is subjected to an elevated temperature of 10 °C.

The objective of this case is to demonstrate the robustness of the NOSBPD formulation in handling discontinuities in a thermomechanical problem by capturing the complex stress behavior induced by the presence of a slit and the temperature-induced softening of the material.

The results of the simulation are presented in Figures 9–12. Figure 9 shows the displacement profiles along two horizontal and two vertical paths. These paths were selected to examine the variations in displacement both near and away from the central slit, providing insight into how the presence of the slit influences the plate's overall deformation. In Figure 10, the displacement fields u_x and u_y in the plate are shown. These show the horizontal and vertical displacements throughout the plate, facilitating for a clear visualization of how the applied displacement at the top edge affects the material points near the slit and across the entire plate.

Figure 11 shows the stress fields σ_{xx} and σ_{yy}, which represent the normal stresses in the horizontal and vertical directions, respectively. These stress distributions allow us to observe the stress concentrations that develop around the slit, particularly near the crack tips, where the stress magnitudes are expected to be significantly higher. Lastly, Figure 12
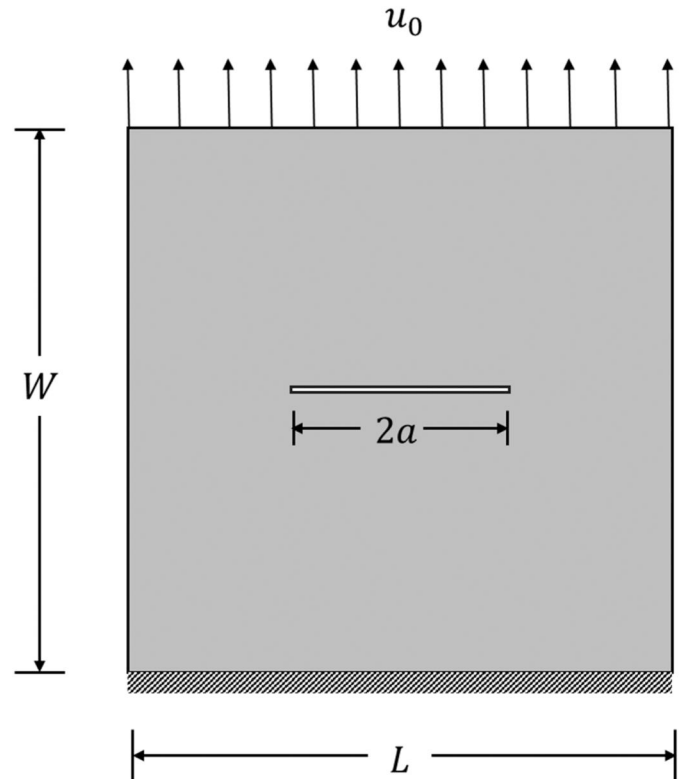

Figure 9. A plate with a slit at the Ccenter.

presents the stress profile along a vertical path that passes by the crack tip. This path is critical for examining the stress intensity near the discontinuity, providing a more detailed view of how the stresses increase in the vicinity of the slit (Figure 13).

The analysis of the displacement and stress fields predicted by the Non-Ordinary State-Based Peridynamics (NOSBPD) reveals some insights into its performance and accuracy, when compared with FEM predictions. The NOSBPD method demonstrates good agreement with FEM in both displacement and stress fields.

The prediction of the displacement field by NOSBPD aligns closely with FEM as shown in Figures 9 and 10, suggesting that NOSBPD can capture deformation behaviors in materials subjected to external forces.
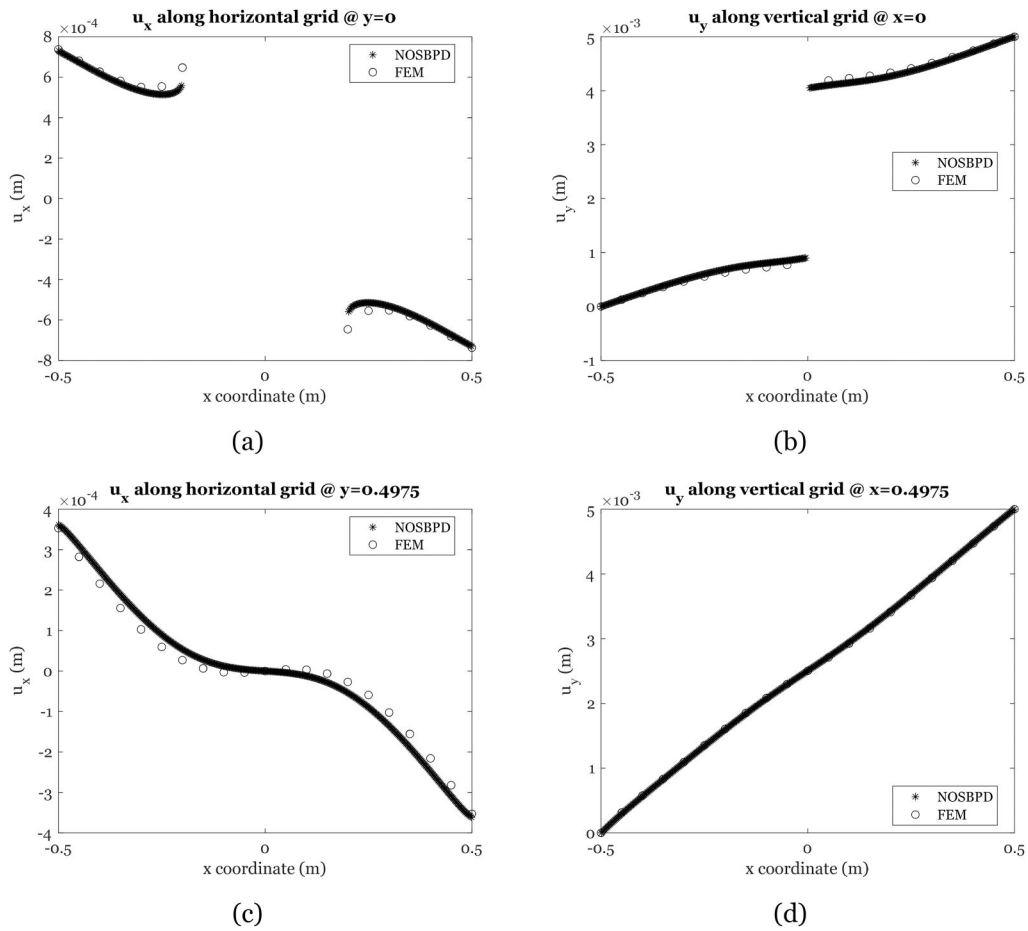
Figure 10. Displacement profiles: (a) u_x along a horizontal path at $y = 0$ (b) u_y along a vertical path at $x = 0$ (c) u_x along a horizontal path at $y = 0.4975$ (d) u_y along a vertical path at $x = 0.4975$.
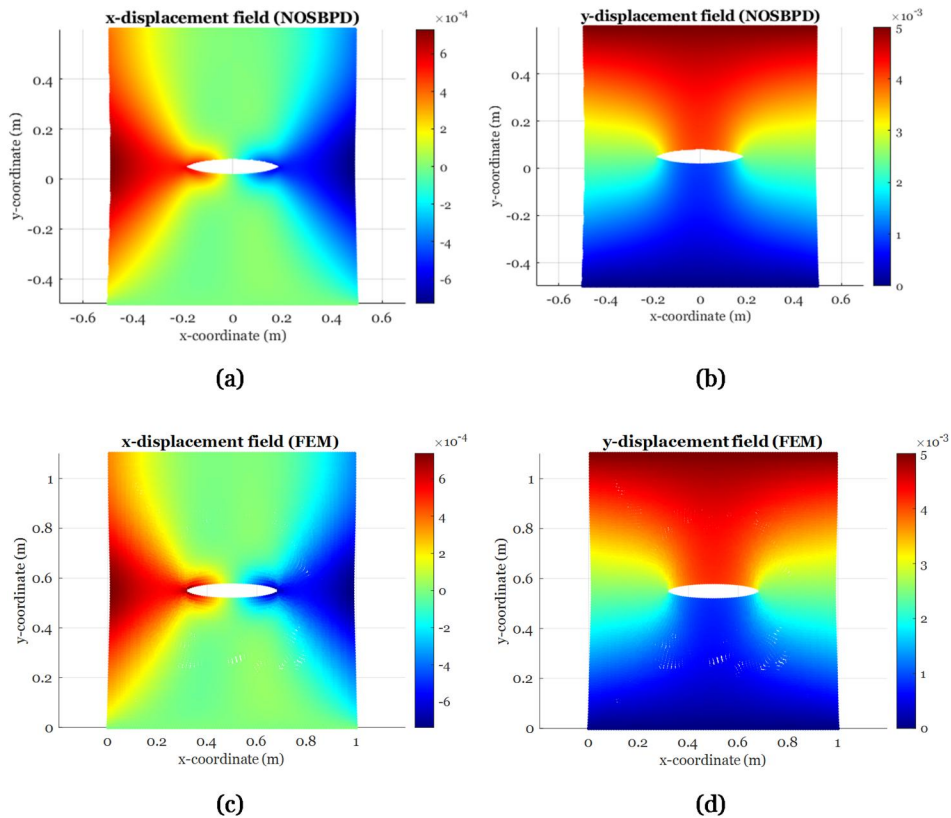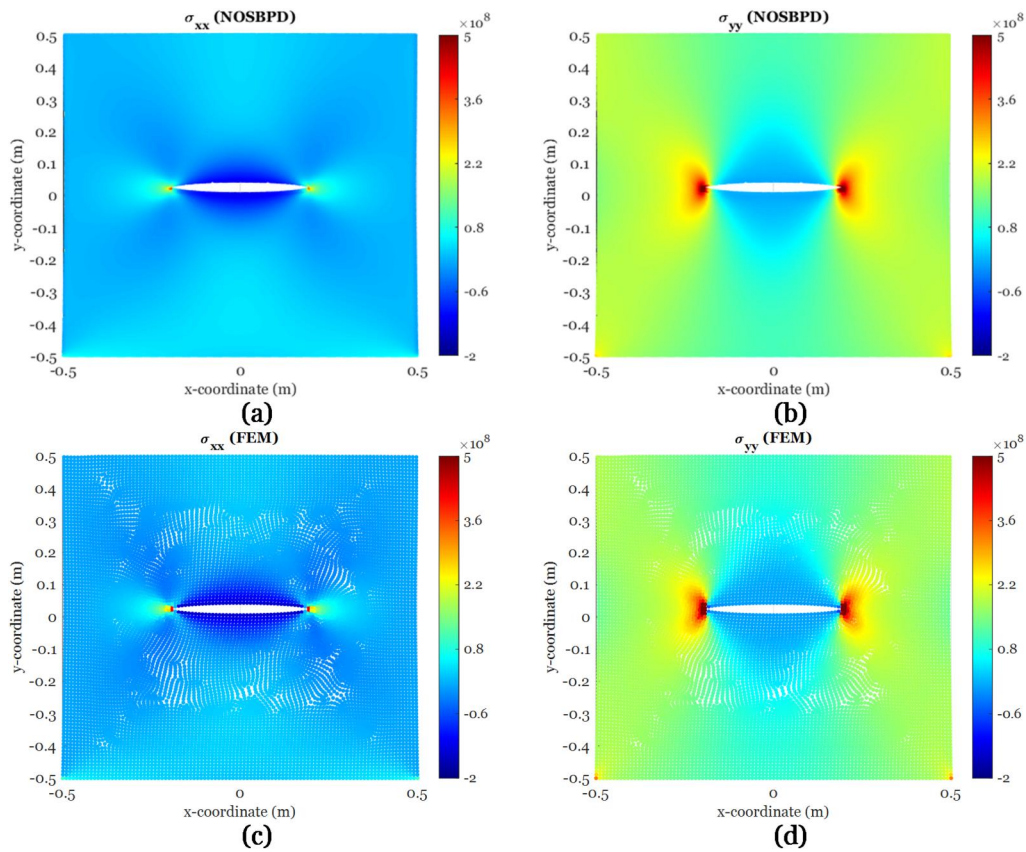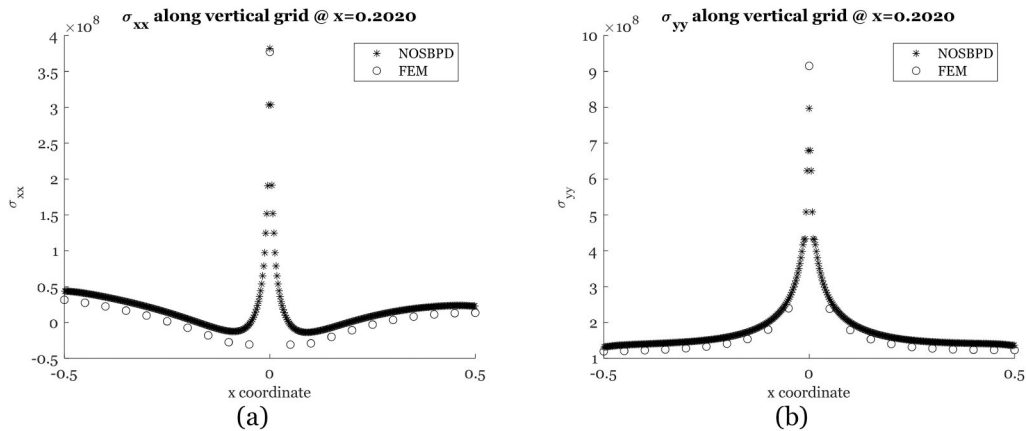

Figure 11. Contour plot of displacement fields (a) u_x prediction from NOSBPD (a) u_y prediction from NOSBPD (c) u_x prediction from FEM (d) u_y prediction from FEM.

Figure 12. Contour plot of stress fields (a) σ_{xx} prediction from NOSBPD (a) σ_{yy} prediction from NOSBPD (c) σ_{xx} prediction from FEM (d) σ_{yy} prediction from FEM.

Figure 13. Stress profile along a vertical path at $x = 0.020$.

The stress field prediction, particularly around the crack tip, is crucial for assessing the method's capability to model fracture mechanics accurately. The results presented in Figure 12 show that the stress components σ_{xx} and σ_{yy} follow a trend that mirrors what is expected in a classical fracture mechanics scenario, with increasing values near the crack tip, indicating stress concentration, and then a rapid reduction as we move away from the crack tip.

The ability of the NOSBPD to produce results that agrees with FEM predictions suggests that it is a powerful tool for analyzing stress fields in problems with discontinuities, such as cracks, offering a reliable alternative or complement to

traditional methods like FEM, particularly for applications where non-local interactions cannot be neglected or when dealing with dynamic crack scenarios

4.3. Response of a plate with a circular hole

In this numerical experiment, we simulate the mechanical response of a steel plate with a central circular hole under varying thermal and mechanical loading conditions. The objective of this simulation is to investigate the effect of elevated temperatures on the force–displacement relationship of the plate. The plate is square, with dimensions of $L = W = 1$ m. A circular hole with a radius of 0.2 m is

located at the center of the plate. The mechanical properties of the steel plate are as follows: an elastic modulus of 210 GPa, Poisson's ratio of 0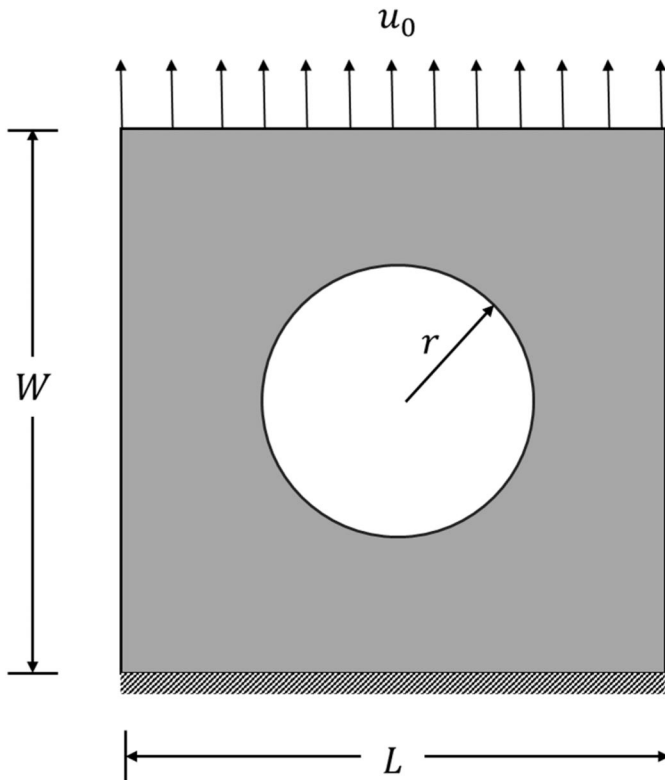.3, and a coefficient of thermal expansion of 12×10^{-6} /°C. Plane stress conditions are assumed throughout the simulation.

For the purpose of the numerical simulation, the plate is discretized into a grid of 301 material points along both the length and width directions, while the thickness direction is represented by a single material point. The plate is fixed along its bottom edge, and a prescribed displacement is applied incrementally along the top edge, as depicted in Figure 14. The applied displacement ranges from 6×10^{-7} m to 6×10^{-5} m over the course of the simulation.

To study the effect of temperature on the mechanical response, the plate is subjected to elevated temperatures of 10 °C, 20 °C, 50 °C, 80 °C, and 100 °C. The thermal expansion of the material is incorporated into the model to observe the temperature-dependent effects on the force–displacement behavior.

The results of the numerical simulation are presented in Figures 15–19. These results show the displacement and stress fields, as well as the temperature-dependent force–displacement relationships for the steel plate.

Figure 15 shows the displacement profile along four different paths on the plate. Two horizontal paths are taken at the coordinates $[-0.5 \leq x \leq 0.5, \; y = 0]$ and $[-0.5 \leq x \leq 0.5, \; y = 0.4975]$, while two vertical paths are taken at $[x = 0, \; -0.5 \leq y \leq 0.5]$ and $[x = 0.4975, \; -0.5 \leq y \leq 0.5]$. The displacement results obtained from the NOSBPD simulation are compared with corresponding results from FEM simulation along these paths.

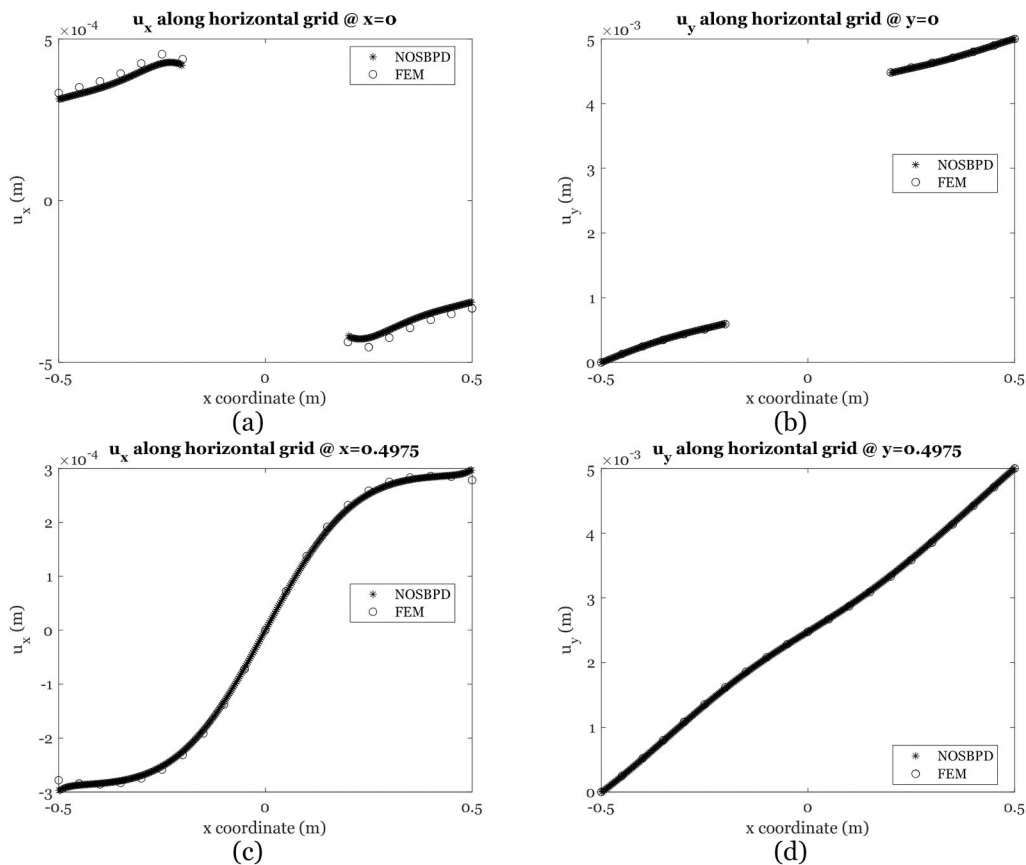

Figure 14. Plate with hole.

Figure 15. Displacement profile along horizontal and vertical paths.

Figure 16(a and b) shows the contour plots of the displacement field in the x and y directions, respectively, as obtained from the NOSBPD simulation. For comparison, Figure 16 (c and d) provides the corresponding displacement contours from the FEM simulation. These plots visually demonstrate the deformation patterns of the plate under the applied displacement load and temperature conditions, highlighting the similarity in the deformation profiles between the two methods.

Figure 17 presents the stress profile along the path defined by $[-0.5 \leq x \leq 0.5, \quad y = 0]$ and $[-0.5 \leq x \leq 0.5,$

$y = 0.4975]$, comparing the results obtained from the NOSBPD simulation with those from the FEM simulation. In Figure 18, contour plots of the stress field are presented for both the NOSBPD and FEM simulations. These plots provide a comprehensive view of the stress distribution across the entire plate. All data presented in Figures 15–18 were taken for an applied displacement of $u_0 = 6 \times 10^{-5}$ m and a temperature of $80\,°C$.

Finally, Figure 19 shows the force-temperature curves for the plate at three different applied displacements: $u_0 = 6 \times 10^{-7}$ m, $u_0 = 3.03 \times 10^{-5}$ m, and $u_0 = 6 \times 10^{-5}$ m.

(a)

(b)

(c)

(d)
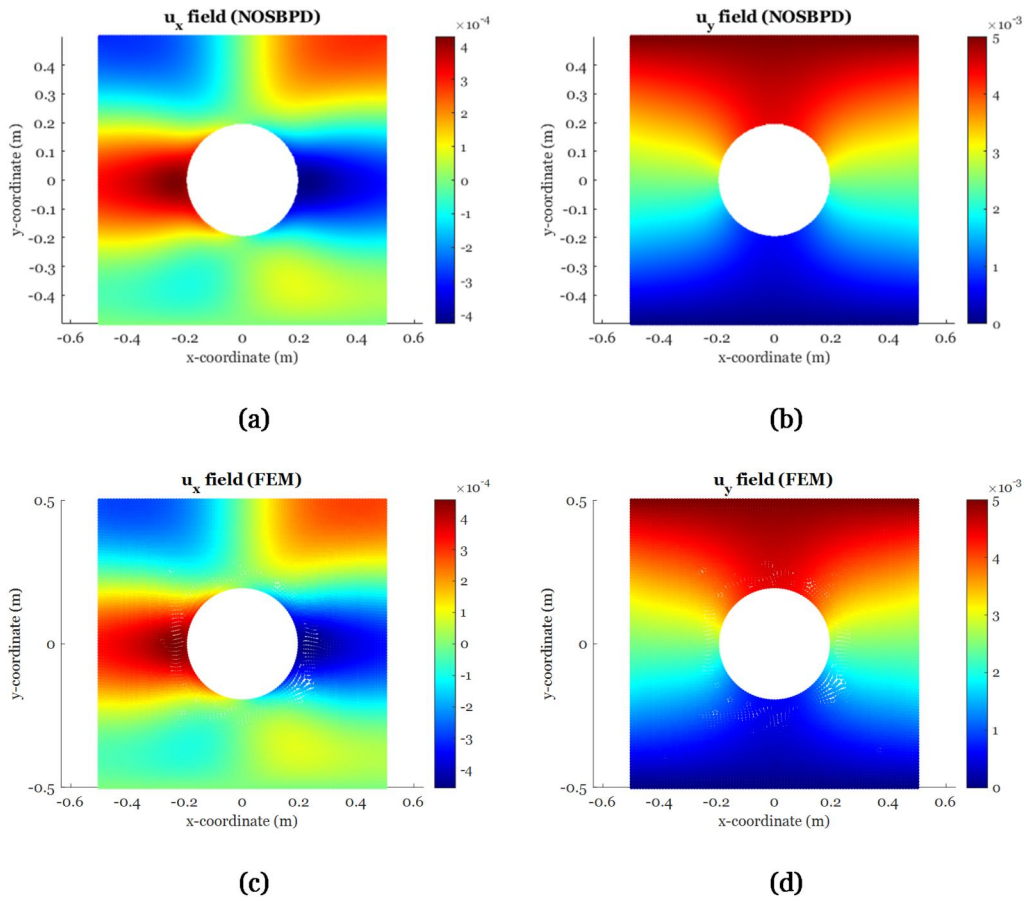
Figure 16. Displacement field at $U_0 = 6.0E\text{-}5$ m and $T = 80\,°C$.
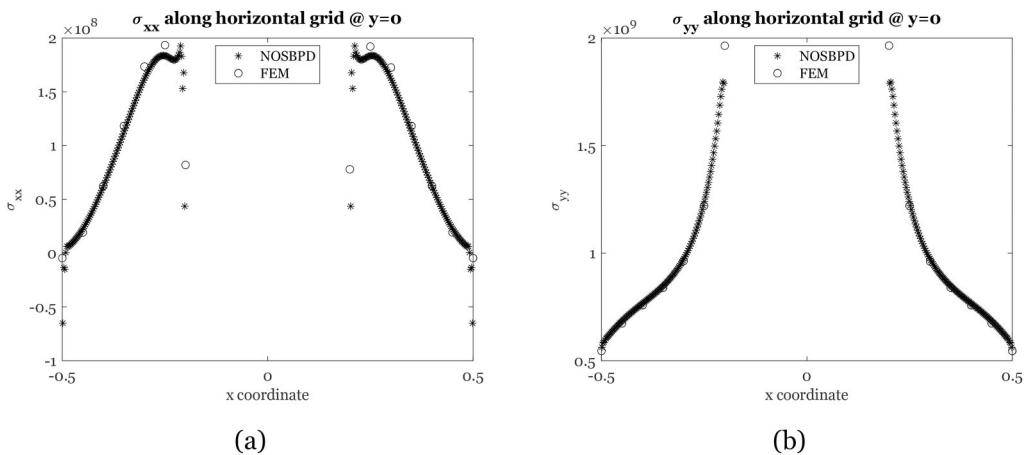

(a)

(b)

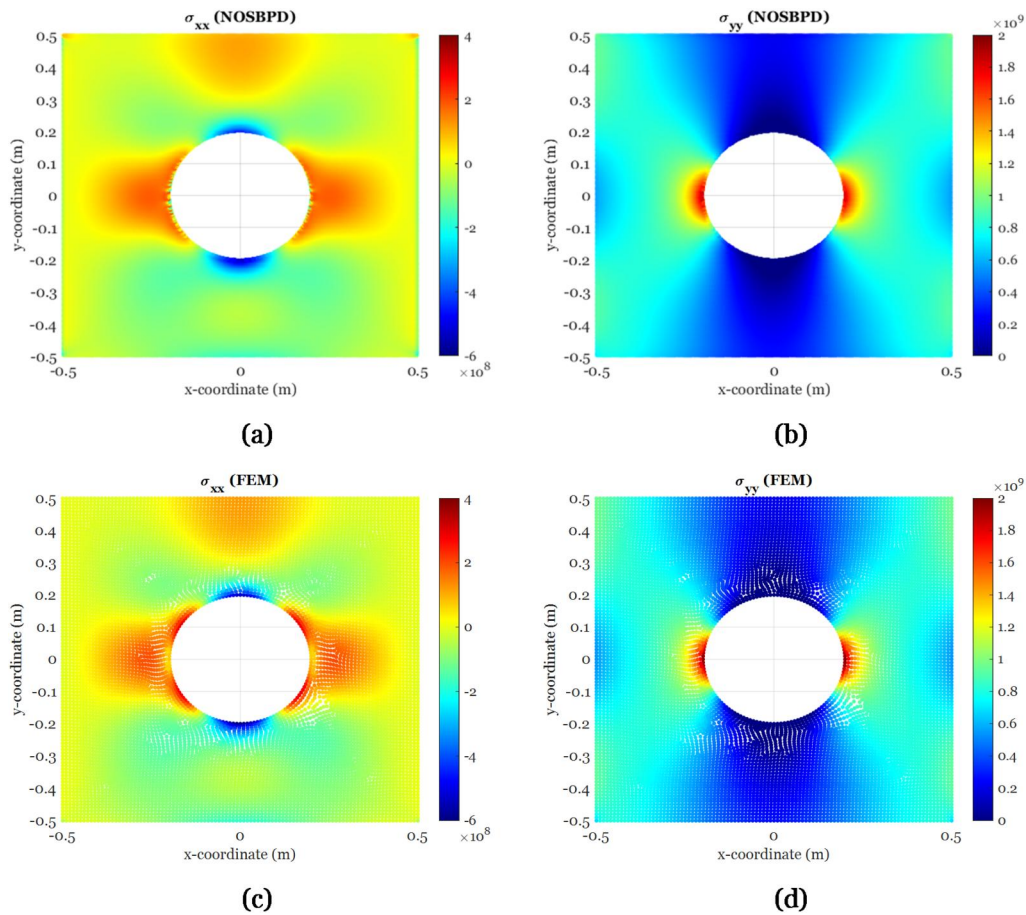**Figure 17.** Stress profile along a horizontal path.

Figure 18. Contour plot of stress field.

These curves illustrate the variation in the reaction force as a function of temperature for each constant displacement.

The results of the simulations obtained using the NOSBPD framework show a strong agreement with those from the FEM simulations across all metrics evaluated, highlighting the accuracy and robustness of the NOSBPD approach in simulating thermomechanical behavior.

The displacement profiles along the horizontal and vertical paths, as shown in Figure 15, reveal that the NOSBPD model captures the displacement distribution accurately when compared with FEM results. This consistency is further reinforced by the contour plots of the displacement field in both the x and y directions as shown in Figure 16, where the NOSBPD and FEM simulations exhibit very similar deformation patterns in the plate in response to both mechanical loading and thermal expansion.

The stress profiles presented in Figure 17 also demonstrate good agreement between the NOSBPD and FEM models. This is further corroborated by the stress contour plots in Figure 18, where the stress distribution across the plate is consistent between both methods, validating the ability of the NOSBPD model to simulate complex stress fields, including those around geometric discontinuities.

The force-temperature curves in Figure 19 show an expected trend in the force–displacement relationship: for a specified temperature, the reaction force increases as the applied displacement increases. This behavior is expected
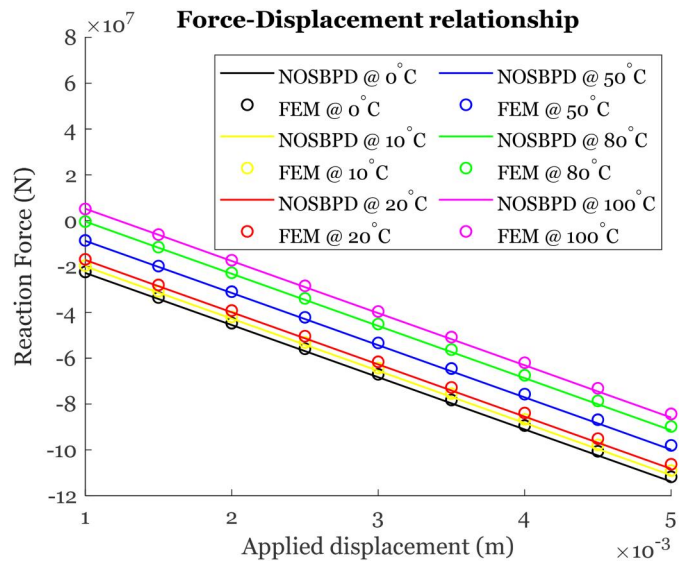

Figure 19. Force displacement relations as a function of temperature.

due to the tensile forces generated as the plate is stretched. At each temperature, the increase in displacement load leads to a corresponding increase in reaction force, consistent with the material's resistance to deformation under the applied mechanical load. This trend is observed in both the NOSBPD and FEM simulations, which demonstrate a strong agreement across all displacement steps.

Table 1. Analysis of force–displacement relationship of the plate.

Applied displacement (m)	Reaction (N) @ 0 °C (NOSBPD)	Reaction (N) @ 0 °C (FEM)	Reaction (N)@ 100 °C (NOSBPD)	Reaction (N)@ 100 °C (FEM)	% Error at 0 °C	% Error at 100 °C
1.00E-03	-2.28×10^7	-2.24×10^7	-2.74×10^7	-2.62×10^7	1.79	4.58
1.50E-03	-3.42×10^7	-3.35×10^7	-2.71×10^7	-2.61×10^7	2.09	3.83
2.00E-03	-4.55×10^7	-4.47×10^7	-2.68×10^7	-2.64×10^7	1.79	1.52
2.50E-03	-5.69×10^7	-5.59×10^7	-2.64×10^7	-2.61×10^7	1.79	1.15
3.00E-03	-6.83×10^7	-6.71×10^7	-2.61×10^7	-2.58×10^7	1.79	1.16
3.50E-03	-7.97×10^7	-7.82×10^7	-2.58×10^7	-2.56×10^7	1.92	0.78
4.00E-03	-9.11×10^7	-8.94×10^7	-2.55×10^7	-2.53×10^7	1.90	0.79
4.50E-03	-1.02×10^8	-1.01×10^8	-2.52×10^7	-2.50×10^7	0.99	0.80
5.00E-03	-1.14×10^8	-1.12×10^8	-2.49×10^7	-2.47×10^7	1.79	0.81

The results also demonstrate the effect of temperature on the force–displacement behavior. As the temperature increases from 0 °C to 100 °C, the magnitude of the negative reaction force decreases. This is due to the thermal expansion of the plate, which induces internal compressive stresses at the fixed edge that act in opposition to the tensile forces generated by the applied displacement. As the temperature increases, these compressive forces increase, reducing the overall magnitude of the negative reaction force at the fixed boundary. This is evident in the upward shift of the force–displacement curve at higher temperatures, where the net reaction force becomes less negative for the same displacement. The NOSBPD model captures this temperature-dependent behavior effectively, as demonstrated by the comparison with FEM results.

A comparative analysis between the results of reaction forces computed by NOSBPD and FEM for various displacement loads and temperature conditions is presented in Table 1. The result show good agreement between predictions from NOSBPD and FEM simulations. The force–displacement curves for both methods follow similar trends, with the percentage error between the two approaches remaining within 1–5%.

5. Conclusion

In this work, we proposed a coupled framework that integrates the PD heat transport model with an implicit NOSBPD thermomechanical model. This framework was applied to three benchmark problems to evaluate its accuracy and effectiveness in simulating thermomechanical behavior in materials.

The first benchmark problem involved a plate subjected to a thermal boundary condition. The PD thermal model successfully simulated the evolution of the temperature field within the plate, and this temperature field was subsequently used as input for the thermomechanical simulation. The displacement field obtained from the thermomechanical simulation showed excellent agreement with results from a FEM simulation of the same problem, validating the accuracy of the proposed coupled framework.

In the second benchmark problem, a plate with a slit was subjected to a prescribed displacement boundary condition. The response of the plate at elevated temperature was simulated. This result highlights the ability of the framework to predict the thermomechanical response of materials, especially in scenarios with geometric discontinuities.

In the third benchmark problem, a plate with a circular hole was subjected to an increasing prescribed displacement boundary condition at elevated temperatures. The temperature-dependent response was successfully simulated, further demonstrating the framework's capacity to handle complex geometries while capturing the influence of elevated temperatures on material deformation.

In conclusion, the proposed coupled PD heat transport and NOSBPD thermomechanical framework has been shown to accurately simulate thermomechanical behavior, offering a reliable tool for modeling complex responses in materials. In future work, we hope to apply this framework to study thermomechanical responses in the presence of dynamic crack propagation.

References

[1] Y. Wang, X. Zhou, and M. Kou, A coupled thermo-mechanical bond-based peridynamics for simulating thermal cracking in rocks, Int. J. Fract., vol. 211, no. 1–2, pp. 13–42, 2018. DOI: 10.1007/s10704-018-0273-z.

[2] J. Amani, E. Oterkus, P. Areias, G. Zi, T. Nguyen-Thoi, and T. Rabczuk, A non-ordinary state-based peridynamics formulation for thermoplastic fracture, Int. J. Impact Eng., vol. 87, pp. 83–94, 2016. DOI: 10.1016/j.ijimpeng.2015.06.019.

[3] S. Bazazzadeh, F. Mossaiby, and A. Shojaei, An adaptive thermo-mechanical peridynamic model for fracture analysis in ceramics, Eng. Fract. Mech., vol. 223, p. 106708, 2020. DOI: 10.1016/j.engfracmech.2019.106708.

[4] Z. Yang, Y. Zhang, and P. Qiao, An axisymmetric ordinary state-based peridynamic model for thermal cracking of linear elastic solids, Theor. Appl. Fract. Mech., vol. 112, p. 102888, 2021. DOI: 10.1016/j.tafmec.2020.102888.

[5] S. Oterkus, E. Madenci, and A. Agwai, Fully coupled peridynamic thermomechanics, J. Mech. Phys. Solids, vol. 64, pp. 1–23, 2014. DOI: 10.1016/j.jmps.2013.10.011.

[6] Y. Song, S. Li, and Y. Li, Peridynamic modeling and simulation of thermo-mechanical fracture in inhomogeneous ice, Eng. Comp., vol. 39, no. 1, pp. 575–606, 2023. DOI: 10.1007/s00366-022-01616-7.

[7] Z. Yang, S.-Q. Yang, and M. Chen, Peridynamic simulation on fracture mechanical behavior of granite containing a single fissure after thermal cycling treatment, Comput. Geotech., vol. 120, p. 103414, 2020. DOI: 10.1016/j.compgeo.2019.103414.

[8] M. Li, W. Lu, E. Oterkus, and S. Oterkus, Thermally-induced fracture analysis of polycrystalline materials by using peridynamics, Eng. Anal. Boundary Elem., vol. 117, pp. 167–187, 2020. DOI: 10.1016/j.enganabound.2020.04.016.

[9] S. Liu, F. Han, X. Deng, and Y. Lin, Thermomechanical peridynamic modeling for ductile fracture, Materials, vol. 16, no. 11, pp. 4074, 2023. DOI: 10.3390/ma16114074.

[10] B. Wang, S. Oterkus, and E. Oterkus, Thermomechanical phase change peridynamic model for welding analysis, Eng. Anal. Boundary Elem., vol. 140, pp. 371–385, 2022. DOI: 10.1016/j.enganabound.2022.04.030.

[11] A. Pathrikar, S.B. Tiwari, P. Arayil, and D. Roy, Thermomechanics of damage in brittle solids: a peridynamics model, Theor. Appl. Fract. Mech., vol. 112, p. 102880, 2021. DOI: 10.1016/j.tafmec.2020.102880.

[12] Y. Gao, and S. Oterkus, Ordinary state-based peridynamic modelling for fully coupled thermoelastic problems, Continuum Mech. Thermodyn., vol. 31, no. 4, pp. 907–937, 2019. DOI: 10.1007/s00161-018-0691-1.

[13] E. Yousefimiab, M.F. Basoglu, and A. Kefal, Peridynamic analysis of thermomechanical effects in fracture toughening mechanisms of stop holes, Eng. Fract. Mech., vol. 301, pp. 110054, 2024. DOI: 10.1016/j.engfracmech.2024.110054.

[14] B. Kilic, and E. Madenci, Peridynamic theory for thermomechanical analysis, IEEE Trans. Adv. Packag., vol. 33, no. 1, pp. 97–105, 2010. DOI: 10.1109/TADVP.2009.2029079.

[15] S. Oterkus, E. Madenci, and A. Agwai, Peridynamic thermal diffusion, Comput. Phys., vol. 265, pp. 71–96, 2014. DOI: 10.1016/j.jcp.2014.01.027.

[16] S.A. Silling, Reformulation of elasticity theory for discontinuities and long-range forces, J. Mech. Phys. Solids., vol. 48, no. 1, pp. 175–209, 2000. DOI: 10.1016/S0022-5096(99)00029-0.

[17] S. Oterkus, and E. Madenci, Peridynamic modeling of fuel pellet cracking, Eng. Fract. Mech., vol. 176, pp. 23–37, 2017. DOI: 10.1016/j.engfracmech.2017.02.014.

[18] M.F. Basoglu, Z. Zerin, A. Kefal, and E. Oterkus, A computational model of peridynamic theory for deflecting behavior of crack propagation with micro-cracks, Comput. Mater. Sci., vol. 162, pp. 33–46, 2019. DOI: 10.1016/j.commatsci.2019.02.032.

[19] Y.K. Galadima, W. Xia, E. Oterkus, and S. Oterkus, Peridynamic computational homogenization theory for materials with evolving microstructure and damage, Eng. Comput., vol. 39, no. 4, pp. 2945–2957, 2022. DOI: 10.1007/s00366-022-01696-5.

[20] X. Song, and N. Khalili, A peridynamics model for strain localization analysis of geomaterials, Num. Anal. Meth. Geomech., vol. 43, no. 1, pp. 77–96, 2019. DOI: 10.1002/nag.2854.

[21] R. De Borst, L.J. Sluys, H.-B. Muhlhaus, and J. Pamin, Fundamental issues in finite element analyses of localization of deformation, Eng. Comput., vol. 10, no. 2, pp. 99–121, 1993. DOI: 10.1108/eb023897.

[22] S.A. Silling, M. Epton, O. Weckner, J. Xu, and E. Askari, Peridynamic states and constitutive modeling, J. Elasticity, vol. 88, no. 2, pp. 151–184, 2007. DOI: 10.1007/s10659-007-9125-1.

[23] P. Li, Z.M. Hao, and W.Q. Zhen, A stabilized non-ordinary state-based peridynamic model, Comput. Methods Appl. Mech. Eng., vol. 339, pp. 262–280, 2018. DOI: 10.1016/j.cma.2018.05.002.

[24] X. Chen, and M. Gunzburger, Continuous and discontinuous finite element methods for a peridynamics model of mechanics, Comput. Methods Appl. Mech. Eng., vol. 200, no. 9–12, pp. 1237–1250, 2011. DOI: 10.1016/j.cma.2010.10.014.

[25] H. Wang, and H. Tian, A fast Galerkin method with efficient matrix assembly and storage for a peridynamic model, Comput. Phys., vol. 231, no. 23, pp. 7730–7738, 2012. DOI: 10.1016/j.jcp.2012.06.009.

[26] M.L. Parks, R.B. Lehoucq, S.J. Plimpton, and S.A. Silling, Implementing peridynamics within a molecular dynamics code, Comput. Phys. Commun., vol. 179, no. 11, pp. 777–783, 2008. DOI: 10.1016/j.cpc.2008.06.011.

[27] S.A. Silling, and E. Askari, A meshfree method based on the peridynamic model of solid mechanics, Comput. Struct., vol. 83, no. 17–18, pp. 1526–1535, 2005. DOI: 10.1016/j.compstruc.2004.11.026.

[28] G.I. Evangelatos, and P.D. Spanos, A collocation approach for spatial discretization of stochastic peridynamic modeling of fracture, J. Mech. Mater. Struct., vol. 6, no. 7–8, pp. 1171–1195, 2011. DOI: 10.2140/jomms.2011.6.1171.

[29] H. Wang, and H. Tian, A fast and faithful collocation method with efficient matrix assembly for a two-dimensional nonlocal diffusion model, Comput. Methods Appl. Mech. Eng., vol. 273, pp. 19–36, 2014. DOI: 10.1016/j.cma.2014.01.026.

[30] N.A. Hashim, W.M. Coombs, C.E. Augarde, and G. Hattori, An implicit non-ordinary state-based peridynamics with stabilised correspondence material model for finite deformation analysis, Comput. Methods Appl. Mech. Eng., vol. 371, pp. 113304, 2020. DOI: 10.1016/j.cma.2020.113304.

[31] M.S. Breitenfeld, P.H. Geubelle, O. Weckner, and S.A. Silling, Non-ordinary state-based peridynamic analysis of stationary crack problems, Comput. Methods Appl. Mech. Eng, vol. 272, pp. 233–250, 2014. DOI: 10.1016/j.cma.2014.01.002.

[32] P. Li, Z. Hao, S. Yu, and W. Zhen, Implicit implementation of the stabilized non-ordinary state-based peridynamic model, Numer. Meth. Eng., vol. 121, no. 4, pp. 571–587, 2020. DOI: 10.1002/nme.6234.

[33] F. Bobaru, and M. Duangpanya, A peridynamic formulation for transient heat conduction in bodies with evolving discontinuities, Comput. Phys., vol. 231, no. 7, pp. 2764–2785, 2012. DOI: 10.1016/j.jcp.2011.12.017.

[34] F. Bobaru, and M. Duangpanya, The peridynamic formulation for transient heat conduction, Int. J. Heat Mass Transf., vol. 53, no. 19–20, pp. 4047–4059, 2010. DOI: 10.1016/j.ijheatmasstransfer.2010.05.024.

[35] L. Wang, J. Xu, and J. Wang, A peridynamic framework and simulation of non-Fourier and nonlocal heat conduction, Int. J. Heat Mass Transf., vol. 118, pp. 1284–1292, 2018. DOI: 10.1016/j.ijheatmasstransfer.2017.11.074.

[36] Y. Tan, Q. Liu, L. Zhang, L. Liu, and X. Lai, Peridynamics model with surface correction near insulated cracks for transient heat conduction in functionally graded materials, Materials, vol. 13, no. 6, pp. 1340, 2020. DOI: 10.3390/ma13061340.

[37] Y. Mikata, Peridynamics for heat conduction, J. Heat Transfer, vol. 142, no. 8, 2020, 081402. DOI: 10.1115/1.4047058.

[38] A. Jafari, R. Bahaaddini, and H. Jahanbakhsh, Numerical analysis of peridynamic and classical models in transient heat transfer, employing Galerkin approach, Heat Trans. Asian Res., vol. 47, no. 3, pp. 531–555, 2018. DOI: 10.1002/htj.21317.

[39] Y. Liao, L. Liu, Q. Liu, X. Lai, M. Assefa, and J. Liu, Peridynamic simulation of transient heat conduction problems in functionally gradient materials with cracks, J. Therm. Stress., vol. 40, no. 12, pp. 1484–1501, 2017. DOI: 10.1080/01495739.2017.1358070.

[40] Z. Chen, and F. Bobaru, Selecting the kernel in a peridynamic formulation: a study for transient heat diffusion, Comput. Phys. Commun., vol. 197, pp. 51–60, 2015. DOI: 10.1016/j.cpc.2015.08.006.